REPORT DOCUMENTATION PAGE

1. REPORT DATE (DD-MM-YYYY) 24/May/2001	2. REPORT TYPE THESIS	3. DATES COVERED (From - To)

4. TITLE AND SUBTITLE
FABRICATION OF CERAMIC MATRIX COMPOSITE TUBES USING A POUROUS MULLIT/ALUMINA MATRIX AND ALUMINA /MULLITE FIBER

5a. CONTRACT NUMBER

5b. GRANT NUMBER

5c. PROGRAM ELEMENT NUMBER

6. AUTHOR(S)
CAPT RADSICK TIMOTHY C

5d. PROJECT NUMBER

5e. TASK NUMBER

5f. WORK UNIT NUMBER

7. PERFORMING ORGANIZATION NAME(S) AND ADDRESS(ES)
UNIVERSITY OF CALIFORNIA AT SANTA BARBARA

8. PERFORMING ORGANIZATION REPORT NUMBER
CI01-87

9. SPONSORING/MONITORING AGENCY NAME(S) AND ADDRESS(ES)
THE DEPARTMENT OF THE AIR FORCE
AFIT/CIA, BLDG 125
2950 P STREET
WPAFB OH 45433

10. SPONSOR/MONITOR'S ACRONYM(S)

11. SPONSOR/MONITOR'S REPORT NUMBER(S)

12. DISTRIBUTION/AVAILABILITY STATEMENT
Unlimited distribution
In Accordance With AFI 35-205/AFIT Sup 1

13. SUPPLEMENTARY NOTES

14. ABSTRACT

20010720 007

15. SUBJECT TERMS

16. SECURITY CLASSIFICATION OF:			17. LIMITATION OF ABSTRACT	18. NUMBER OF PAGES	19a. NAME OF RESPONSIBLE PERSON
a. REPORT	b. ABSTRACT	c. THIS PAGE		71	19b. TELEPHONE NUMBER (Include area code)

UNIVERSITY OF CALIFORNIA

Santa Barbara

Fabrication of Ceramic Matrix Composite Tubes Using a Porous

Mullite/Alumina Matrix and Alumina/Mullite Fiber

A thesis submitted in partial satisfaction of the

requirements for the degree of Master of Science

in Materials

by

Timothy Carl Radsick

Committee in Charge:

Professor Fred F. Lange, Chair

Professor Frank W. Zok

Professor Carlos G. Levi

June 2001

The thesis of Timothy Carl Radsick is approved:

_____

Professor Frank W. Zok

_____

Professor Carlos G. Levi

_____

Professor Fred F. Lange, Committee Chair

May 2001

Fabrication of Ceramic Matrix Composite Tubes Using a Porous

Mullite/Alumina Matrix and Alumina/Mullite Fiber

ABSTRACT

Fabrication of Ceramic Matrix Composite Tubes Using a Porous

Mullite/Alumina Matrix and Alumina/Mullite Fiber

by

Timothy Carl Radsick

Continuous fiber ceramic composites show promise for applications in high-temperature oxidizing environments, but their actual use has been limited in part due to unstable non-oxide-based constituents or from inadequate oxide-based ones. A porous mullite/alumina matrix combined with alumina/mullite fiber reinforcement eliminates the need for an interface coating while producing a strong, tough and oxidation resistant composite. In this study, a fiber-matrix prepreg was produced by infiltrating Nextel 720 cloth with a filter-pressed mullite/alumina slurry through a VibroIntrusion process. This prepreg was used to fabricate thin-walled tubes, which were then pressure burst tested to failure. Post-test evaluation of the tubes and a finite element analysis show that the tubes failed from excessive interlaminar shear stresses. The implications of these results and the utility of the fabrication method used in this study are discussed.

List of Figures

<u>I: Introduction</u>

One of the most significant differences between Ceramic Matrix
Composites (CMCs) and other classes of composite materials (e.g. metal and
polymer matrix composites) is that for CMCs the matrix and fiber are composed of
either the same or similar materials, both of which are brittle. Besides their possible
difference in chemistry, their different processing routes produce a major difference
in their flaw population and, consequently, their strengths. Fibers are produced by a
spinning method and have a diameter that limits their largest flaw, which
determines their lowest strength. The matrix, on the other hand, does not have a
flaw size limit, and thus fails at a much smaller strain than the fibers.

In the fabrication of most fully dense CMCs, some sort of coating is
therefore required to act as a crack deflecting interphase between the fiber and
matrix. The crack deflecting interphase not only ensures that when a crack extends
through the matrix, it does not also extend through the fibers, but it also prevents
the fibers and matrix from sintering together during the high temperature
processing needed to produce the CMC.

In addition to ensuring that high processing temperatures and pressures do
not simply sinter fiber and matrix together into a brittle monolithic ceramic,
coatings themselves serve to deflect cracks, to isolate fiber failure from neighboring
fibers and to promote the dissipation of crack energy through frictional sliding of

failed fiber segments, a process commonly referred to as "fiber pull-out." All these mechanisms provide some degree of damage tolerance in the CMC.

Fiber coatings have been used quite successfully in the fabrication of ceramic composites, most notably using boron nitride or graphite as a coating for SiC or Si_3N_4 fibers. In applications where long-term resistance to high-temperature oxidizing environments is a crucial design goal, however, the use of these non-oxide coatings is counterindicated. Though such coatings may produce initially a CMC with favorable properties, these properties are slowly degraded as matrix microcracking allows oxidation of the coatings to take place. Thus in order to use CMCs in aerospace engine or power generation applications, oxidation and subsequent reduction in properties must be either eliminated or another CMC concept used.

Perhaps the most obvious solution to come to mind would be the use of oxide-based interphase between the fiber and matrix. A few oxide coatings have been developed which show some promise in laboratory-scale produced samples, including monazite[1], porous zirconia[2], hexaluminates/magnetoplumbites.[3, 4] These coatings, however, are not without their own set of problems, including processing issues such as application of the coating, retention of the coating during matrix incorporation and densification, reactions between fiber/coating/matrix, etc. In addition, deposition of fiber coatings can be an expensive and time-consuming process, increasing the total life cycle cost of CMC components in real-world application.

While continued work on these fiber coatings is likely to yield improved results, incremental improvements may not yield the final properties desired in all high temperature oxidizing applications, a possible Xeno's paradox where progress is made toward a goal but at an ever diminishing rate. Thus it is prudent to evaluate other CMC concepts that can exhibit damage tolerance and long-term oxidation resistance and that can do so at a reasonable life-cycle cost. One such possibility is the use of porous matrices to provide crack deflection and damage tolerance, completely eliminating the need for a fiber coating. In a general sense, a porous matrix acts in much the same way as does an interphase layer: deflecting cracks away from fibers and transferring load in the presence of damaged fibers. In the case of a porous matrix, however, these effects arise from the entire matrix, not just in the localized region between fiber and matrix.

II: Background

(A)   Behavior of Ceramic Matrix Composites

The reduction in maximum flaw size brought about through the use of small diameter ceramic fibers was mentioned earlier in this paper. Such a reduction in flaw size is in itself a beneficial property for a material, but more important for CMCs is the toughness provided by having fibers somewhat "isolated" from the

matrix and from neighboring fibers, thus enabling cracks to be deflected rather than progressing directly from matrix into fiber.

He and Hutchinson analyzed the case of cracks terminating at an interface and found that the ratio of the interface fracture energy, Γ_i, to the mode I fracture energy of the fiber, Γ_f, could be used to predict debonding conditions.[5] Figure 1 shows a plot of the energy release ratio versus elastic mismatch, α, given by:

$$\alpha \equiv \frac{\left(\bar{E}_f - \bar{E}_m\right)}{\left(\bar{E}_f + \bar{E}_m\right)} \tag{1}$$

where $\bar{E}_f$ is the plane strain modulus of the fiber and $\bar{E}_m$ is the plane strain modulus of the matrix. The plot illustrates a critical ratio of Γ_i/Γ_f above which cracks penetrate into the fiber and below which fibers debond from the matrix. For materials with small values of elastic mismatch, as is the case with CMCs, the critical fracture energy ratio is approximately 0.25.

In the case of a fiber and a fully dense matrix made from the same material with the same microstructure, it is easy to see that the fracture energy ratio between the two will not be 0.25, but instead will approach 1.0 and that the elastic mismatch parameter will be approximately zero. The only major difference between the properties of the fiber and the matrix would be flaw size and population. Thus such a material will fail much like a monolithic ceramic. Fibers will fail in a correlated manner, manifesting a highly planar fracture surface. Such a material would have a

4

low degree of toughness. In order to avoid this, some sort of isolation between neighboring fibers is required in order to provide a mismatch in properties and thus bring about crack deflection.

This "isolation" can be achieved in several ways. Phillips demonstrated one of the first engineered CMCs, a carbon fiber reinforced glass, which used no coatings or porosity to separate fiber from matrix. Rather, in this material, the weak bond between carbon and glass provided the required isolation.[6] In effect, fiber and matrix were mechanically bonded but chemically unbonded. Crack deflection at the fiber/matrix interface was natural since it more than satisfied the He and Hutchinson criteria. These very early CMCs processed by Phillips et al exhibited a high degree of toughness, equal to that of advanced CMCs produced much later.

An extension of this case would be the use of carbon, or a material with a similarly weak bond to the matrix, as a fiber coating. Thus non-carbon fibers could be used, with the interface layer providing isolation due to a difference in fracture energy and in elastic properties. Such a material would end up with a non-zero elastic mismatch and a fracture energy ratio less than 1. Depending on the material chosen for the interphase, such a CMC could behave in either a brittle manner (no debonding) or with demonstrated toughness (resulting from debonding.)

Unfortunately as discussed earlier, these interphase coatings historically have been non-oxide based materials such as carbon or BN. Candidate oxide coatings tend to have difficulty meeting the requirements of uniform deposition, tailorability, and low cost. In addition, many candidate oxide coatings do not have

significant differences in elastic properties and fracture energy, and thus do not directly create a ideal condition where debonding will easily occur.[2, 3, 4] Rather, the effects of porosity in the interphase create a debonding condition. A natural extension of this interphase porosity would be to simply make the matrix itself porous and eliminate the need for an interphase layer.

(B) Porous Matrix Concept

Porous matrices represent a third type of CMC, and though the failure of a porous matrix CMC differs from that of conventional dense matrix CMCs,[7] fibers are still isolated from one another, insuring that failure of a single fiber does not directly lead to the failure of neighboring fibers due solely to the presence of a stress concentration at the crack tip. Rather, near a failed fiber, the matrix will serve to transfer load to surrounding fibers, which in turn will fail in a non-correlated manner, determined mainly by the load carried and the flaw population of the fibers.[8]

(C) Purpose of Study

The purpose of this study was threefold:

(1) To evaluate the efficacy of the porous matrix concept in the
manufacture of a specimen other than a planar laminate

(2) To develop simple, low-cost processing methods which could be
used in a later cost-effective manufacture of production specimens.

(3) To demonstrate the usefulness of the VibroIntrusion process in the
fabrication of CMC prepregs.

After careful consideration, a tube was selected as the specimen
configuration for several reasons. First, though a tube is a complex shape, it is
basically an extension of a flat panel laminate curved upon itself. More complex
parts may also be candidates for the use of porous matrices and VibroIntrusion
(through filament winding possibly), but their manufacture is beyond the scope of
this effort. A tube is also a good choice due to it's applicability to possible real-
world uses, including high-temp power piping in power generation, and tubular
combustors or curved combustor liners in turbine engines. Finally, a tubular shaped
specimen opens up the possibility of using pressure testing to determine material
properties.

(D) Matrix Concept in Study

The matrix chosen for this study was composed of a binary mixture of 70
vol% mullite and 30 vol% alumina in an aqueous slurry. After undergoing a

sintering step, the matrix forms an arrangement of large mullite particles bound together and connected to fibrous reinforcement by a network of connective alumina bridges. Porosity remains unchanged during the heat treatment required to sinter the alumina particles, provided that this heat treatment does not enable the mullite particles to sinter as well.

Neither dispersive chemicals nor surfactants were added to this slurry. Rather, the Derjaguin-Landau-Verwey-Overbeek theory of colloidal stability ("DLVO Theory") was used to create a weakly attractive particle network where the long-range, power-law van der Waals attraction is summed with a short-range double-layer repulsion.[9] Through the addition of base and salt, the pH and the ion content of the slurry were adjusted to control the formation of a counterion cloud around each particle. As particles, attracted by van der Waals interaction, approach one another, their counterion clouds overlap creating a region of increased ion concentration. Thus an increase in energy is required to bring the particles together. At large separations, this increase in energy is more than compensated for by the decrease in energy due to van der Waals interaction. At the point where these two energy functions balance one another, a secondary minimum is created in the interparticle potential (primary minimum is at particle contact). Slurry particles are thus attracted to each other by van der Waals interactions, but prevented from coming into contact with each other due to electrostatic double layer repulsion.[10] Figure 2 illustrates this interparticle potential.

In addition to the electrostatic double layer repulsion, steric repulsion was also utilized through the adsorption of large molecules to the surface of the matrix particles. These molecules provide an additional repulsive force that initiates once the adsorbed molecules come into contact or interpenetrate one another. This steric hindrance further prevents the slurry particles from overcoming the energy barrier between primary and secondary potential minimums, and thus coming into direct contact.[10] The purpose of this manipulation of interparticle pair potential is to create a colloidal suspension with a large volume fraction of suspended solids but with favorable rheology for subsequent fiber infiltration using a filter-pressed slurry.

Pressure filtration is an effective method to pack particles densely around fibers with a very high packing density. In pressure filtration, a fiber preform is placed into a die cavity containing a fine-scale filter (usually at one end of a cylindrical cavity.) Slurry is introduced to the cavity and pressure applied, causing liquid to be forced out through the filter and leaving behind a layer of solid particles on the filter. As more and more fluid is pressed out through the filter, the thickness of the particle layer increases according to Darcy's Law, eventually incorporating the fiber reinforcement into the layer of particles. Once a consolidated layer of particles extends from the filter surface to the opposite end of the die cavity, pressure is removed and the green body CMC is removed and dried. This process works well for producing flat panel configurations using slurries with highly repulsive particle potentials.

VibroIntrusion is modification of this filter-pressing technique where only the slurry undergoes pressure filtration. The consolidated body is fluidized by vibration and used to infiltrate a fiber preform. Careful control of the interparticle potential determines the rheology of the consolidated slurry so that it can be easily infiltrated into fibers.[11] VibroIntrusion is a more flexible process than direct pressure filtration; for example, the fluidized slurry can be used to infiltrate fiber preforms of complex shape and configuration. In addition, the infiltrated fibers remain flexible and can be used to form complex shapes after matrix infiltration, opening up the possibility of using manufacturing techniques generally used for PMC manufacture (e.g. fiber-matrix prepregs, filament wet winding, etc.)

Because of the subsequent flexibility of the impregnated fiber, VibroIntrusion can be used to simply and cost-effectively fabricate CMC tubing. In the technique used for this study, a filter-pressed slurry was used to infiltrate by VibroIntrusion a single layer of woven ceramic fiber cloth. This layer of cloth was then rolled around a collapsible mandrel (Figure 3), additional vibration and compression were applied to consolidate the CMC layers with one another, and after drying the mandrel was removed. Subsequent infiltration with alumina precursors allows the matrix porosity and strength of the alumina connecting bridges to be tailored.

Once fabricated, the tubular configuration of the specimens lends itself to testing of the specimens using hydrostatic burst testing. In either test, tubes are simply mounted into a test fixture that will close off the open ends of the tube,

creating a pressure vessel with end constraints. Pressurized gas or liquid is used to apply a hydrostatic stress to the tube enabling calculation of material properties. Notched specimens can be prepared by either machining a groove partially through the thickness of the tube, or by coring a hole through the tube and sealing off the hole to maintain pressure in the tube. This test method shows promise as an alternative to determine tensile properties relative to that of using a tensile test specimen prepared from flat panel laminates.

III: Experimental Materials and Methods

(1) Materials

All specimens prepared in this study used Nextel 720™ alumina/mullite fiber in an eight-harness satin weave as reinforcement. Sizing applied to the fabric by the manufacturer was removed through thermal treatment in air at 900°C for a period of 2 hours; otherwise the fabric was used in the as-received condition.

Nextel 720 fibers are composed of approximately 85 wt% Al_2O_3 and 15 wt% SiO_2 in the form of submicron-sized grains of mullite and alumina. This composition provides improved creep resistance relative to Nextel 610™ alumina fiber but with a 30% decrease in mean filament strength at ambient temperature.[12,13] Approximately 400 fibers comprise a tow.[14] The fiber length within a tow, per unit mass, was measured (using a cloth sample of known

dimensions) to be 5980m/kg, which agrees with the published value of ~6000m/kg.[14,15]

The particle sizes and particle size distributions of mullite and alumina powders used in this study were selected to insure relatively high packing densities of the final filter-pressed slurry. The mullite powder selected was MU-107 (Showa Denko KK, Tokyo Japan) with a mean particle size (as determined by the manufacturer) of $1\mu m$ and a particle size distribution of 0.5-2.5 μm. An α-alumina powder (AKP-50, Sumitomo Chemicals, Tokyo, Japan) was used with a mean particle size (determined by the manufacturer) of $0.2\mu m$ and a particle size distribution of 0.1-0.3μm.

An alkoxide precursor for aluminum oxide, Aluminum-*sec*-butoxide, $Al(OC_4H_9)_5$ (Sigma-Aldrich, St Louis, MO), was used to infiltrate and strengthen the matrix with three infiltration and pyrolysis cycles. The precursor was used without added solvent. The precursor is 97% pure and yields 20.1% Al_2O_3 by weight after pyrolysis, assuming complete oxidation of Al and no vaporization loss of Al. Infiltration was performed in a dry nitrogen atmosphere to prevent premature gelation of the precursor due to atmospheric water vapor.

(2) Slurry Preparation

Aqueous slurries were prepared with a 20% volume content of solids, comprising 70 vol% mullite and 30 vol% alumina. The mullite-to-alumina ratio

12

was selected to insure sufficient alumina was present to form connective sintering necks between mullite particles.[15] Tetramethylammonium hydroxide (TMA-OH) was used initially, and in all subsequent steps, to maintain the pH above 11. Zeta-potential measurements on mullite and alumina powders showed that pH 11 was sufficient to insure a dispersed slurry. Two weight percent of N-(Triethoxysilylpropyl)-O-polyethylene oxide urethane (PEG-Silane, Gelest Inc.) was added to induce a steric effect due to the adsorption of molecules by a reaction with –OH surface sites on both powders. Slurries were stirred and sonicated for 10 minutes and placed on a mechanical roller for approximately 12 hours. After mixing, tetramethylammonium nitrate (TMA-N) salt was added to make a 0.25 molar solution. The TMA^+ counterions cause the PEG steric molecules on the surface to condense, producing a short-range repulsive potential, and thus a weakly attractive particle network. Slurries were returned to the mechanical roller for another 12 hours.

Slurries were poured into a 45mm diameter die cavity and consolidated by pressure filtration at 4 MPa until the plunger motion was negligible for a 10-minute period. The pressure filtration period was approximately 3 hours for the consolidation of 40ml of slurry. The consolidation pressure of 4 MPa was below the critical pressure where a large number of particles are pushed into contact, which would obviate fluidization after consolidation.[16] The resulting disks of consolidated matrix material were removed from the filter press and sealed in plastic bags. A combination of manual shear manipulation and mechanical

13

vibration were used until the consolidated bodies were completely fluidized. Later, a corner of the bag was cut and used in the manner of a pastry bag to dispense the fluidized body onto the fiber cloth. The weight difference method was used to determine the relative density of the fluidized consolidated bodies.

(3) Composite Tube Manufacturing

The fiber cloth was cut into 10.2 cm x 7.6 cm specimens (4.0 x 3.0 inches); the two outermost tows along all four edges were manually removed to help eliminate stray fibers. Additional tows were removed from the longer sides until a 0.64 mm (0.25-inch) "extension tab" was created at each end as shown in Figure 5. A 7.6 cm x 8.9 cm (3 x 3.5 inch) plastic strip (cut from disposable plastic bag) was attached using strips of cellophane tape to one of the extension tabs of each cloth specimen. The role of the plastic tabs was to aid in fastening the fiber cloth to the mandrels used to roll the cloth, and to facilitate the removal of the mandrel once the specimen was dried.

The fiber/tab pieces were placed in a plastic bag and an excess of the fluidized body was dispensed to both sides of the fiber cloth. The plastic bag served to prevent the slurry from drying and from adhering to tools used in subsequent manufacture. Assisted by vibration, the slurry was manually rolled across the surface of the fiber with a piece of aluminum rod and until the cloth was fully infiltrated. Excess slurry was removed by rolling it from the surface of the cloth to

distant portions of the plastic bag. The thickness of the fiber cloth itself determined the resulting thickness of the prepreg layer. Any deviations in prepreg layer thickness manifested clearly as white-colored regions and could be subsequently eliminated by targeted rolling and vibration until a consistent color and weave pattern was observed.

Prepreg layers were placed on a metal block cooled with dry ice, frozen, removed from the plastic bag, and placed between pre-cut strips of plastic. Freezing facilitated the removal of the prepreg from the plastic bag. The extension tab attached to the prepreg was clamped into a three-part collapsible mandrel made of stainless steel shown in Figure 5. The prepreg was kept frozen during this step by keeping it on the cold metal block, as illustrated in Figure 6. The extension tab was then wound up tightly around the mandrel until the mandrel reached the frozen prepreg. At this point, the initial matrix/cloth section was slid away from the metal block, placed atop a vibrating aluminum table at room temperature, and the upper layer of protective plastic sheet was removed.

As the matrix material thawed and became fluid once again, the prepreg section was slowly wound around the mandrel. Gentle pressure was applied to the prepreg in order to squeeze out a small portion of the fluid powder matrix and create a wake of matrix just in front of the composite tube that was forming around the mandrel. This wake of matrix slurry served to fill in air gaps as the prepreg layer wrapped on itself, thus preventing large scale porosity in the final composite.

Once the cloth was fully wound around the mandrel, the strip of protective plastic was tightly wrapped around the prepreg tube, and the resulting mandrel-specimen unit was vibrated for 3-4 minutes to improve consolidation and to allow excess matrix to be squeezed from the cloth by applied pressure. After the vibration was completed, strips of rubber were wound around the mandrel from the center outward and the entire assembly was again vibrated for 3-4 minutes and then placed in a drying oven at 80°C. After one hour of heating, the rubber strips and protective plastic were removed, allowing the specimen to completely dry.

Once the specimen was dry, the mandrel was collapsed and removed from the inside of the composite tube. Tubes were heated to 900°C for 2 hours to burn out the plastic extension tab and cellophane tape and to partially sinter the alumina particles to the mullite particles. This stabilized the porous matrix for subsequent infiltration with the alumina precursor.

The tubes were placed into glove box containing a dry nitrogen atmosphere to prevent gelation of the alkoxide alumina precursor contained within the chamber. After evacuating the chamber, the tubes were immersed in the alkoxide precursor and the vacuum removed. The tubes were left in the precursor for 2 minutes at atmospheric pressure, and then removed from the glove box. The tubes were placed into ammoniated water (pH 10) to gel the precursor throughout the body and prevent it from re-distributing to the surface during the evaporation of the solvent.[17],[18] After 30 minutes, tubes were removed, dried and heated to 900°C in order to first pyrolyze and crystallize the precursor, and then densify it to bond

together the mullite particles. In this manner, the density of the matrix and the strength of the connection between mullite particles could be increased, with no shrinkage. This infiltration and pyrolysis step was repeated three times. In between each cycle, excess alumina on the surface, which arose from a surface layer of gelled precursor, was removed by gently rubbing the inner and outer surfaces with a soft cloth.

After the third infiltration cycle, the specimens were heated to 1200°C in order to densify the alumina between the mullite particles. Several tubes were prepared to determine the notch sensitivity of the CMC material. In these tubes, a diamond coring bit was used to core a 0.125-inch hole at the center of the tube. The inside of the tube near the hole was coated with a compliant epoxy and sealed by a plate of material from another CMC tube. Figure 7 shows a normal and cross sectional view of this configuration.

(4) Testing

Brass testing fixtures, illustrated in Figure 8, were prepared to enable pressure testing of the CMC tubes. Tubes were joined to the test fixtures using a rapid curing epoxy resin (Figure 9.) The testing fixtures were designed so that tubes of different finished lengths nonetheless could be tested having similar gauge length. Several of the test-fixture/CMC-tube assemblies were connected to a 137.5 KPa (20 psi) Nitrogen source allowing the permeability of the CMC to be measured

17

by immersion in water and subsequent measurement of the volume of gas passing through the material.

Internal pressure was applied to the CMC tube from a helium source. Pressure was increased at approximately 100 KPa/s until a loud and distinct audible crack occurred, and at approximately 70 KPa/s afterwards until the tube failed. Five specimens were tested; a sixth specimen was tested with a core-drilled hole. The first three tubes were tested with a controllable flow restrictor in the pressure line. Once the tube reached its failure pressure, a pressure drop was recorded that closed the restrictor to prevent the volume of gas in the test apparatus from rushing out of the failed tube and causing further damage. In this testing mode, the location where the specimen failed could be determined. The final three specimens were tested without this the restrictor device in order to better see the consequence of a failed composite tube.

IV: Results

(1) Tube Specifications

The length of the tubes fabricated by the described method varied between 6.1 to 7.9 cm and their inner diameter averaged 1.28 cm. The thickness of all the tubes was determined to be 0.049 cm +/- 0.02. The tubes were composed of two layers of cloth and were produced by winding an initial single strip of prepreg cloth

around the mandrel two times. The small section of the tube (less than 1/5th of its circumference) where ends of the cloth overlapped contained three layers of cloth. All thickness measurements were made in the 2-layer region of the tube.

The relative density of the matrix prior to heat treatment was measured through a weight difference method, namely, specimens of consolidated slurry were weighed, allowed to dry, fired at 800° C to burn off residual water, silane dispersant and TMA salt, and then reweighed. For the purpose of calculation, a value of 1.09 g/cc was used for the density of the TMA-N salt and the silane dispersant. Packing density was thus determined to be 56±1%. After three cycles of precursor infiltration and pyrolysis, this value increased to 64.1%. The increase in weight was assumed to be due to the addition of AlO_2 from the Alumina precursor -- this addition of alumina caused a shift in mullite-to-alumina volume ratio from 70/30 to approximately 67/33. Using the volume fractions of the different constituents, the fiber volume fraction in the final composite was determined to be 0.39.

(2) Testing

The permeability of two tubes was measured to be 1.1 l/s m² at 137.5 KPa (20psi). The permeability of the remaining tubes could not be determined accurately; one had a pinhole leak at the brass mount and several others had residual epoxy that sealed off an undetermined portion of their surface.

Pressure testing resulted in the observation of two distinct failure events. The gas pressure where a distinct audible crack was first heard (Failure Event 1) was hypothesized to be associated with a delamination event. This failure event occurred at an internal pressure of 1.77 ± 0.5 MPa. At this point, no audible increase in gas leakage was detectable and additional internal pressure could be applied to the CMC tubes. The fact that the tube continued to hold pressure suggested that either the delamination crack had not progressed entirely through the tube, or the tube was completely delaminated but remained intact due to friction, layer stiffness and the epoxied ends.

In tests performed with the restrictor valve, which prevented the sudden release of gas during ultimate failure (Failure Event 2), it was evident the specimens failed by a delamination crack that spiraled between the wrapped CMC layers, appearing to propagate inward from the outer layer to the inner layer. This failure event occurred at an average applied pressure of 3.00 ± 0.21 MPa. The post-failure specimens retained their tubular shape. Fracture surfaces could be seen only by manipulating the specimen, thereby causing the prepreg coil to slightly unwrap. There appeared to be some damage at the epoxy interface, which might account for the distinction between Failure Events 1 and 2.

One possibility is that Failure Event 1, as discussed earlier, signaled the fast progression of an interlaminar crack though the tube, though the tube held together due to the epoxied ends and the constraints they applied to the tube. Failure Event 2

signaled a slight separation of the CMC layers from the epoxy end constraints, thus allowing internal pressure to escape through the interlaminar crack region.

In tubes tested without the flow restrictor the release of pressurized helium in the test apparatus caused the tubes to blow apart catastrophically, as shown in Figure 10. The fibrous fracture and extensive fiber exposure result from the outward flow of helium after Failure Event 2. Though the post-test appearance of tubes tested with and without the flow restrictor appear dramatically different from one another, tube failure is still assumed to occur initially via interlaminar shear with no fiber pullout; only subsequent damage differs between the two.

The core-drilled tube was tested in an identical manner to the pristine tubes. In this case, however, Failure Event 1 occurred at an internal pressure of 2.39 MPa and Failure Event 2 at 6.34 MPa. This counterintuitive increase in strength is discussed below.

V: Modeling and Discussion of Stress State

Due to the complex geometry of the fabricated tubes, the constraints of the brass fixtures and the anisotropy and radial inhomogeneity of the CMC material, an explicit elastic solution of the stress conditions is not feasible without an extensive stress analysis that is beyond the scope of this work. Nevertheless, simplified physical models and Finite Element Modeling (FEM) techniques provide insight

into the stress state of the pressurized CMC tubes and thus into the modes of failure.

(1) Ideal Thin-walled Cylindrical Pressure Vessels with Free Ends

The stress state in a long thin-walled tubular pressure vessel with free ends is well known[19], with hoop stress given by

$$\sigma_{hoop} = \frac{pr}{t} \qquad (2)$$

where

σ_{hoop} = circumferential normal stress
p = internal pressure
r = radius and
t = thickness of the tube wall.

The addition of free end caps introduces an additional axial stress, σ_a given by[20]

$$\sigma_{axial} = \frac{pr}{2t} \qquad (3)$$

For the standard tubes tested in this study, by substituting the tube dimension and failure pressures into eq. (3), one would calculate a normal hoop stress of 23.5 ± 7.0 MPa for Failure Event 1 and 38.9 ± 2.7 MPa for Failure Event 2. It is useful to compare these results to those predicted from a theoretical tube (henceforth referred to as "ISO Tube") made of a material with orthotropic properties determined using a rule-of-mixtures treatment of fiber and matrix.

Independent studies have shown that the preprocessing fiber bundle strength of Nextel 720 is ~800-900 MPa.[14, 15] Using a fiber bundle strength of 850 MPa, 0°/90° fiber orientation, a 40% fiber volume fraction and a highly porous matrix, one would expect failure to occur at a material stress of 170 MPa which translates into an internal pressure of 13 MPa, a pressure 7.2 times the pressure causing Failure Event 1. Though 170MPa is most likely optimistic, other researchers have produced similar materials with strengths of 130-150 MPa.[14, 15] Thus this simple model of an idealized tube does not adequately model the tested tubes, suggesting that other considerations must be taken into account.

(2) Thin-walled Cylindrical Pressure Vessels with "Built In" Ends

One such consideration is that the actual stress condition of the tubes fabricated for this study includes additional constraints on the tube ends, commonly referred to as a "built in" or cylindrically-cantilevered condition. This condition is illustrated in Figure 11. These additional radial and axial constraints are such that total radial deformation, ω, and the slope of the radial deformation, $d\omega/dz$, must both be zero at each constrained end. As a result, a radially symmetric shear stress and bending moment are introduced at each end. Such a loading condition on a tube can be analyzed using an elastic continuum mechanics model[21, 22, 23] that is summarized in the following paragraphs.

An analysis of the equations of equilibrium and an application of symmetry relationships results in the following three equations:

$$\frac{dN_z}{dx} = 0 \tag{4}$$

$$\frac{dQ_z}{dx} + \frac{1}{r}N_\varphi = p \tag{5}$$

$$\frac{dM_z}{dx} - Q_z = 0 \tag{6}$$

where

N_z and N_φ = normal forces in the axial and circumferential directions, respectively,
Q_z = transverse shear force,
M_z = bending moment about a circumferential axis, and
p = Internal Pressure.

An application of Hooke's Law and a symmetry argument that the change in curvature in the tube in the circumferential direction equals zero, gives

$$N_\varphi = -\frac{Et\omega}{r} \tag{7}$$

$$M_\varphi = \nu M_z \tag{8}$$

$$M_z = -D\frac{d^2\omega}{dz^2} \tag{9}$$

where D is the rigidity of the tube and is given by

$$D = \frac{Et^3}{12(1-\nu^3)}.$$

Combining Equations (4)-(9) and assuming constant thickness of the tube wall

gives

$$\left(D\frac{d^4\omega}{dz^4}\right)+\left(\frac{Et}{r^2}\omega\right)=-p \tag{10}$$

the general solution of which equation is given by

$$\omega = e^{\beta z}\left(C_1\cos\beta z + C_2\sin\beta z\right) \\ + e^{-\beta z}\left(C_3\cos\beta z + C_4\sin\beta z\right)+f(z) \tag{11}$$

where

$$\beta = \sqrt[4]{\frac{Et}{4r^2D}}$$

and f(z) is the particular solution which results from an applied internal pressure.

An application of boundary conditions allows us to solve for the unknown

constants C_n. Assuming that the length of the tube is large, this gives $C_1 = C_2 = 0$

and

$$\omega = \left(\frac{e^{-\beta z}}{2\beta^3 D}\right)\left[\beta M_0(\sin\beta z - \cos\beta z) - Q_0\cos\beta z\right] \tag{12}$$

In this case the circumferential strain, ε_φ, is given by

$$\varepsilon_\varphi = -\frac{\omega}{r} \tag{13}$$

and Hooke's Law allows us to find ε_z, the axial strain

$$\varepsilon_z = \nu\left(\frac{\omega}{r}\right) = -\nu\varepsilon_\varphi \qquad (14)$$

Combining Equations 6, 9 and 12 allows us to determine M_z and Q_z as well.

As in Section (1) above, this stress model can be used to analyze a pressure vessel (ISO Tube.) The epoxy bond to the actual test fixtures is considered to meet the "built-in" conditions for ω, and $d\omega/dz$. Figure 12 plots normal stress versus normalized axial position. As illustrated, the effects of the "built-in" end constraints are localized to each end of the tube and rapidly taper off in a damped oscillation about the far field value (tube center) determined by the particular solution. Between $z/l = 0.1$ and 0.9, end effects have dropped off such that variation in normal stress is $+/-1\%$.

Figure 12 shows that peaks in the normal stress occur at $z/l \approx 0.061$ and 0.939. At the internal pressures used to test the tubes in this study, these peaks have values of 24.5 (Failure Event 1) and 40.5 MPa (Failure Event2) -- results 4.2% greater than the values of 23.5 and 38.9 estimated in Section 1. For the ISO Tubes with an ultimate strength of 170 MPa, failure would be predicted at an internal applied pressure of approximately 12.5 MPa. This approach suggests a 400% difference in actual results and modeled results, showing that a rule-of-mixtures model of the tube is insufficient to predict material stress and determine failure. The "jelly-roll" fabrication of the tubes must be taken into account; specifically the peel and interlaminar shear properties of the laminate material.

(3) Lap Joints and Laminar Stresses

The overlap region of the fabricated CMC tubes is similar in a broad sense to a single-lap joint (Figure 13). Lap joint stresses have been modeled analyzed by a wide range of researchers for the last 60 years, but most of the more recent studies base their efforts on the 1944 work of Goland and Reissner[24] who were the first to take into account the effects due to rotation of the adherends.[25] This study provided the basis for subsequent work, which corrected mistakes and refined the Goland-Reissner models with more valid assumptions and boundary conditions.[26, 27] Tsai and Morton's revised model is used in the following paragraphs to discuss stresses in the overlap region.[28]

Figure 13a shows the configuration of a single-lap joint comprising two adherends and an adhesive layer. Note the deviation of the loading axis from the neutral axis, which will induce a bending moment along the adherends and at the adherend-adhesive interface. A free body diagram of the single-lap joint (Figure 13b) shows the forces and moments that result from an applied tensile load, while Figure 13c illustrates the deformation expected as the loading axis and neutral axes align. This loading configuration results in a peel stress (normal stress tangent to the local plane of the adherends) and an interlaminar shear stress in the adhesive region between the two adherends. The simplified distributions of these stresses are shown in Figures 13d and 13e.

Tsai and Morton show that the peel stress is given by

$$\sigma_{peel} = \left(\frac{Tt}{c^2\Delta}\right)\left[\begin{array}{l}\left(R_2\lambda^2\frac{k}{2} + \lambda k'\cosh\lambda\cos\lambda\right)\cosh\left(\frac{\lambda x}{c}\right)\cos\left(\frac{\lambda x}{c}\right) \\ + \left(R_1\lambda^2\frac{k}{2} + \lambda k'\sinh\lambda\sin\lambda\right)\sinh\left(\frac{\lambda x}{c}\right)\sin\left(\frac{\lambda x}{c}\right)\end{array}\right] \quad (15)$$

with the max peel stress given by

$$\sigma_{peel}^{max} = \left(\frac{Tt}{c^2}\right)\left[\lambda^2\frac{k}{2}\left(\frac{\sinh 2\lambda - \sin 2\lambda}{\sinh 2\lambda + \sin 2\lambda}\right) + \lambda k'\left(\frac{\cosh 2\lambda + \cos 2\lambda}{\sin 2\lambda + \sin 2\lambda}\right)\right] \quad (16)$$

where

$$k = \frac{2M_0}{Tt} \text{ and } k' = \frac{cV_0}{Tt} \quad (17)$$

$$\lambda = \left(\frac{c}{t}\right)\sqrt[4]{\frac{6E_c(1-v^2)t}{E\eta}} \quad (18)$$

$$R_1 = \cosh\lambda\sin\lambda + \sinh\lambda\cos\lambda$$
$$R_2 = \sinh\lambda\cos\lambda + \lambda\cosh\lambda\sin\lambda \quad (19)$$

$$\Delta = \frac{1}{2}(\sinh 2\lambda + \sin 2\lambda) \quad (20)$$

and

T = tensile force per unit width
t = adherend thickness
η= adhesive thickness
2c = adherend overlap

28

E = adherend modulus
E_c = adhesive modulus
v = Poisson's ratio of adherend
M_0 = joint edge moment
V_0 = joint edge shear

where

$$V_0 = \frac{1}{2c}[(t + \eta)T - 2M_0]$$ (21)

Given Tsai and Morton's model and estimated values for the properties of the CMC used in this study (Table 1), the calculated value of applied stress that would cause the joint to peel open is 1.1 MPa, given a matrix strength of 30 MPa. This corresponds to an internal pressure of 79.5 KPa for a built-in tube at Failure Event 1. The actual pressure at Failure Event 1 was 22 times this value. This large discrepancy results in large part from an assumption that the entire applied load transfers from one adherend to the other through the adhesive layer. Because the infiltrated cloth in the fabricated CMC tubes was wound around the mandrel two times, however, there are not two adherends bonded together completely by an adhesive layer. Rather, one infiltrated layer is continuous through the joint region and two adherends are bonded to it, one on either side and at opposite ends. In the joint overlap region, applied tensile loads would be carried largely by this layer. This in turn would reduce the peel stress over that of a simple lap or joggle-lap joint.[29] A more accurate model would take into consideration the load that would

29

be carried by this continuous "adherend". Using a stress relief factor of 0.20, for example, would indicate a pressure at Failure Event 1 of approximately 0.4 MPa.

The above value is a more reasonable one, though this modified Tsai-Morton model is still not entirely applicable to the conditions at failure. There are several other problems with applying the Tsai-Morton model to the CMC tubes. First, this model does not concede that fracture initiates from a pre-existing crack. Since the conception of the model in the 1940's, it is has become well known that fracture strength is governed by pre-existing cracks and the resistance of the material to crack extension. These newer concepts, so widely used today, are not included in this model. Second, in the actual joint in the CMC tubes, the loading and neutral axes are collinear in the region away from the joint, and one "adherend" curves sigmoidally in the region immediately adjacent to the lap. This type of joint is sometimes referred to as a "joggle-lap joint"[29] and is illustrated in Figure 14a-e. Also, the material used in this study is not isotropic. Rather, fiber layers have orthotropic in-plane properties determined by the properties of cloth and matrix, and through-thickness properties determined primarily the matrix. In addition, there is not an adhesive, per se, in the joint region; rather adhesion is determined by the surface layer of porous matrix on each side of the infiltrated cloth layers. These layers extend out past the joint overlap region.

One final difference is that in the fabricated tubes the interior step of the lap joint is somewhat smoothed out by a flow of matrix to this region. This would serve to smooth out the 90° reentrant corner that occurs in a simple lap or joggle-

lap joint and reduce the stress concentrations at this point.[30] A similar effect occurs to a lesser extent on the exterior step.

To better model the stress state on the CMC tubes, these many factors should be taken into account. Accordingly, two separate finite element models of the overlap section were prepared -- one based upon a simple lap joint (skewed loading and neutral axes) and one based on a joggle-lap joint (collinear loading and neutral axes.) These models will be referred to as a "Lap-Type" and a "Joggle-Type" joint. In each model, tube curvature is neglected due to the 13:1 ratio of tube radius to wall thickness. Stress is applied uniformly to each side of the joint at a reasonable distance to ensure Saint Venant's principle applies in the joint region. The applied stress is the peak stress found in the study in Section 2 above for Failure Event 1 for a tube with built-in ends. In reality, this peak stress model applies for only two distinct axial positions on the tube, but the "Lap-type" and "Joggle-Type" models are two dimensional and this peak stress is assumed to be the stress that would first initiate crack formation and progression in the actual tubes. Individual composite layers are modeled as a sandwich of an infiltrated fiber layer between two thin layers of matrix material. This accounts for the laminate structure of the jelly-rolled CMC tubes and the difference between in-plane and through-thickness properties. The properties of both the infiltrated fiber portion and the matrix portion are modeled as being individually isotropic; this assumption does not exactly match the true response of the CMC tube, but greatly simplifies modeling and is sufficient to initially investigate the stress state. Figure 15

31

illustrates the two models, the Lap-Type joint and the Joggle-Type joint, used to investigate the stresses in the CMC tubes.

(4) Finite Element Model of CMC Tube Failure

A finite element analysis of these two joints was conducted using MSC Patran/Nastran software.[31, 32] The finite element meshes of the two models are shown in Figures 16 and 17. A Quad-4 (four node) two-dimensional solid elasticity element in a plane strain condition was used for the model of the lap-type joint. A geometrically linear stress-strain response was selected for the analysis. This same element was used for the majority of the elements in the joggle-type joint, with the exception that periodic quad-stacked triangular elements were used in the triangular joggle-overlap region of the joggle-type joint. This was done to obtain coincident node placement along the transition between the triangular filled-in joggle region and the planar CMC layer. A 90° interface corner was used in the model; no radius in the adhesive layer (spew fillet) was included in either the lap- or joggle-type models to smooth the transition between adherends.[33, 34]

In order to ensure an accurate and useful result, a mesh seed was conducted before final mesh of the FEA models. A relatively course mesh was established in the non-critical regions of the models. In the lap-type model, the horizontal and vertical node density was selected to be 1 node/mm and 67 nodes/mm respectively. In the critical regions of the model (the reentrant corners and the CMC-matrix

32

interfaces in the joint-overlap region) a higher node density was used, specifically 4 nodes/mm and 133 nodes/mm for the horizontal and vertical node density. In the joggle-type model, a variable node spacing auto mesh function was used to increase node density in the joint-overlap region and decrease it at the adherend ends.

A unidirectional tensile stress was applied to each model in the direction of the long dimension of the adherends. In the lap-type joint, the central point in the model was fixed in 2-D space but allowed to rotate. Equal and opposite 12.5N tensile loads were applied to a single point at the center of each free end of the adherends. The magnitude of the force corresponds to the 24.5 MPa stress occurring at Failure Event 1 described above. The application of the force at a single point created large stress concentrations in the region immediately around the point forces, but these rapidly diminished to be unnoticeable in the joint-overlap region. At the point of the applied stresses, additional rotational constraints were added in order to enable solution of the FEM by Nastran software. These constraints should not have been necessary, but error logs generated by Patran prompted their inclusion.

Table 2 lists the material properties used in both models. Filament tensile modulus for Nextel 720 before weaving and processing is reported to be 260 GPa.[14] Thus in a 0°/90° orientation, one would expect the fiber cloth alone to have a modulus of approximately 50 GPa (determined by $E = 0.5 f E_f$, where volume fraction is approximately 0.40 and assuming no contribution from the matrix.) The matrix, though, does contribute to the final modulus, increasing it approximately

33

10% in a porous matrix system such as that used in this study.[15] In addition, though the bulk fiber volume fraction in the composite is 0.39, laminate composites tend to consist of CMC layers with fiber volume fractions higher than the bulk value sandwiched between layers of almost pure matrix (with fiber volume fractions near zero.)[11, 35] The thickness ratio between these two layers varies according to processing techniques, but in this study is estimated to be 6:1. Accordingly, the modulus of the CMC layers is approximately 70-75 GPa. 75GPa was selected as the CMC layer Young's Modulus for the FEA.

The properties of the matrix layer were estimated according to the process used by Lam, et al.[7] A rule of mixtures treatment of the matrix (initially 70% mullite, 30% alumina) would give a 300 GPa modulus for a fully dense matrix. This assumes moduli of 260 and 400 GPa respectively for mullite and alumina. The initial porosity of the matrix in this study should result in a matrix stiffness of between 10% and 15% of the fully dense result. The lower modulus value was chosen, thus 30 GPa was used in the FEA. As will be illustrated later, the interlaminar stresses generated by the model depend on the relationship between the moduli of the CMC and matrix layers. The CMC layer and matrix layer properties taken together would result in a composite material with an overall modulus of approximately 60 GPa. This value compares well with literature values from studies of similar composite composed of Nextel 720 fiber and a porous mullite-alumina matrix. [11, 15]

The resulting peel and interlaminar shear stresses are shown in Figures 18 and 19. Together they illustrate that a delamination crack will initiate and progress inward through the thin layers of porous matrix. The maximum peel and interlaminar stresses generated at the Failure Event 1 hoop stress for the lap-type joint are approximately 16MPa and 68MPa, respectively. Peel and shear stress in the Joggle-Type joint are respectively 4MPa and 20MPa. In each case, the interlaminar shear stress is significantly larger than the normal peel stress. These models more closely match the proposed mechanism of CMC tube failure and account for the low failure pressures of the fabricated tubes. Other researchers have found that the peak shear stresses developed in a similar porous matrix composite are approximately 8 to 10 MPa.[15]

Stresses in the joggle-type joint are lower than those in the lap-type joint due to the relatively collinear loading and neutral axes and the smoothed joint transition resulting from matrix flow to the inner surface of the joint overlap region. In the fabricated tubes, this region was not completely filled in with matrix resulting in a diminished but still noticeable step remained after processing. As a result, the stresses seen by the actual CMC tubes are expected to be somewhere between the values estimated by the two FEA models.

An additional factor worthy of note is the sensitivity of the shear stress in the joggle joint region to the relative moduli of the CMC and matrix layers. A series of FEA models were analyzed having a matrix/CMC modulus ratio ranging from 0.033 to 1.0. A semi-logarithmic plot of the resulting shear stresses is shown

in Figure 20. Small changes in the elastic mismatch ratio can result in rather large changes in the value of shear stress.

The models show that peel stresses are low compared to shear stresses, indicating the CMC tubes fabricated for this study most likely failed due to shear failure of the porous matrix. The shear stress range of the FEM models, 20-68 MPa, matches closely with published values of the strength of porous alumina powder compacts.[7] Most likely the initial failure was due to interlaminar sheer in the joggle region. Once the matrix in the filled-in joggle region failed, a delamination crack rapidly progressed through the porous matrix between the CMC layers (Failure Event 1). The epoxy adhering the ends of the tube to the brass test fixtures prevented complete failure of the tube at this point. Additional pressure was needed to cause the delaminated layers to detach from the fixtures (Failure Event 2)

VI: Discussion of Results

(1) Gas Permeability

The values of gas permeability reported above would be expected of a thin-walled tube with a porous matrix. If intended for use in a gas-tight application, the application of an mullite/alumina sealing layer to the surfaces of the part should help to mitigate the negative effects of porosity. Thicker-walled tubes would also reduce gas permeability. The uniform porosity, though, may be useful in some

applications. The main reason for the use of CMCs in aerospace applications is the need for materials with low thermal expansion coefficients and materials that can withstand high temperatures with a reduced need for cooling fluids. In cases where some use of cooling fluid or the injection of gases through a wall thickness is desired, the porosity of this particular CMC would make it a useful candidate, if critical issues such as fuel penetration and water absorption could be managed. Such applications may include rocket motor injector plates or film-cooled combustion chambers and nozzles, for example.

(2) Pressure Testing

The relatively low burst strength of the CMC tubes most likely can be attributed to the lower strength of the porous matrix, which is the only structural material between the wound prepreg layers. It is known that the shear strength of a similar porous matrix CMC is approximately one-half that of a denser matrix CMC.[36] It is hypothesized that the initial crack forms at the outer surfaces at the "steps" generated by the edges of the spiral wrapped cloth, most likely at the interior joggle surface (Figure 21). At this location, interlaminar shear stress is at a maximum due to a discontinuity in loading -- this stress is relieved through the generation of an interlaminar crack that progresses through the entire tube. As additional pressure is applied, the epoxy bond at the tube ends is damaged and the tube fails by "unrolling" much as a rolled up piece of paper unrolls when released.

37

Thus rather than testing the tensile properties of the CMC, pressurizing the tube to failure tested the peel and interlaminar properties, at least in this instance. One unexpected result, however, was that the delamination crack and the final failure occurred at such different stresses. The tubes ultimately held a pressure that was 40% greater than the pressure causing the delamination crack.

It was originally intended to test a series of tubes containing core-drilled holes to demonstrate the known notch-sensitivity of the porous matrix CMC[36], as well as to show the usefulness of pressure testing in evaluating notch sensitivity. The results of the first of these tests, however, showed a pressure increase of approximately 200 %. This apparent increase in strength was most likely due instead to a combination of two other factors: a decrease in the applied stress in the region of the notch due to the presence of the CMC backing plate and an increase in resistance to interlaminar shear resulting from the bonding of the wound cloth with residual epoxy. This epoxy, which partially filled the cored hole, was used to cement the small piece of CMC over the hole. The first factor would tend to reduce the stress in the tube in the immediate area of the cored hole -- in effect, an additional constraint at the center. (Figure 22) The second factor would tend to resist the progression and opening of an interlaminar crack; an intact epoxy "plug" would act to tie together adjacent lamina. The results of the cored tube pressure test when compared to the results from non-cored tubes illustrate the weakness of the porous matrix in shear and show the usefulness of the introduction of some additional connection between lamina. It is hypothesized that the use of some sort

of fiber reinforcement acting between the fiber layers and interconnecting them would produce significant improvements in the interlaminar shear properties. These improvements likely would not increase the ultimate burst strength of the tubes to the level of a filament-wound tube, but may be sufficient to allow a "jelly-rolled" tube to be useful in lower pressure applications.

VII: Conclusion

The main purpose of this research was to develop and demonstrate the efficacy of a simple, low-cost method to fabricate CMCs having complex shapes. This purpose was achieved, though the fabricated test specimens failed in matrix shear at relatively low applied internal pressures. The matrix concept, a filter-pressed mullite/alumina slurry, provided consistent and relatively high values of packing density, requiring few precursor infiltration steps in order to achieve the desired final density.

VibroIntrusion provided good infiltration of the matrix material into the fiber cloth. Preparation of fiber/matrix prepreg layers was straightforward with fabrication steps much like those used for polymer matrix prepreg material. This similarity highlights the possibility of using this filter-pressed matrix slurry concept in the preparation of prepreg fiber tows, which could then be used to filament wind on a vibrating mandrel. This method would allow the fabrication of even more

complex shapes than a simple tube and would help to resolve the main weakness in the tubes used in this study, the weak interlaminar shear properties.

While the ease of fabrication, consistency and appearance of the completed CMC tubes was notable, the maximum strength values were limited by the porous matrix and by the "jelly-roll" fabrication scheme that created stress discontinuities at the ends of the "roll." A simple spiral-wrapped cloth tube with a porous matrix would be expected to fail through a delamination of the wrapped cloth, as there is no inter-ply reinforcement provided by the fibers. A filament wound tube would largely eliminate this weakness, but significant improvement may be made through the use of small amounts of interply strengthening fibers. This was demonstrated by the increase in burst strength of the core-drilled tube having an epoxy "plug" filling the hole and connecting adjacent layers. Further research into techniques to improve interlaminar shear properties is currently being conducted and will help mature this material and processing concept into one which may be useful for low-pressure thermal protection applications in aerospace propulsion and power generation, as just two examples. Low-cost, ease of fabrication, low-residual stresses, avoidance of coating-issues and an all-oxide composition make this material concept a promising one.

REFERENCES

1. J.B Davis, D.B. Marshall, and P.E.D. Morgan, Monazite-containing Oxide/Oxide Composites, *J. Eur. Ceram. Soc.*, **20**, 583-587 (2000)

2. K. Nubian, et. al., Chemical Vapor Deposition of ZrO2 and C/ZrO2 on Mullite Fibers for Interfaces in Mullite/Aluminosilicate Fiber-reinforced Composites, , *J. Eur. Ceram. Soc.*, **20**, 537-544 (2000)

3. M.K. Cinibulk and R.S. Hay, "Textured Magnetoplumbite Fiber-Matrix Interphase Derived from Sol-gel Fiber Coatings", *J. Am. Ceram. Soc.*, **79**, 1233-1246 (1996)

4. L. Meyer, B. Saruhan, and H. Schneider, Development of Lanthanumhexaluminate Fiber-Coating via Sol-Gel-Route Using Inorganic and Organic Precursors, *Key Engineering Materials Vols 164-165*, pp 53-58 (1999)

5. M.Y. He and J.W. Hutchinson, Crack Deflection at an Interface Between Dissimilar Elastic Materials", *Intnl. J. of Solid Structures*, **25**, 1053-1067 (1989)

6. D.C. Phillips, "Interfacial Bonding and the Toughness of Carbon Fiber Reinforced Glass and Glass-Ceramics", *J. of Mat. Sci.*, **11**, 1847-54 (1974)

7. D.C.C. Lam, F.F. Lange, and A.G. Evans, "Mechanical Properties of Porous, Alumina Ceramics Produced from Powder Compacts, " *J. Am. Ceram. Soc.,* **77** [8] 2113-17 (1994)

8. F.W. Zok and C.G. Levi, Mechanical Properties of Porous-Matrix Ceramic Composites, submitted to *Advanced Engineering Materials,* March 2000

9. J. Israelachvili, Intermolecular and Surface Forces, 1992 Academic Press Ltd, pg 241-249

10. F.F. Lange, C.G. Levi, and F.W. Zok, Processing Fiber Reinforced Ceramics with Porous Matrices, Chapter 14 in *Comprehensive Composite Materials,* ed. by R. Warren, Elsevier Press, 2000

11. J.J. Haslam, K.E. Berroth, and F.F. Lange, Processing and Properties of an All-oxide Composite with a Porous Matrix , *J. Eur. Ceram. Soc.,* **20,** 607-18 (2000)

12. D.M. Wilson, S.M. Lieder, and D.C. Lueneburg, Microstructure and High Temperature Properties of Nextel 720 Fibers, *Cer. Eng. Sci. Proc.,* **16,** 1005-1014 (1995)

13. D.M. Wilson, Statistical Tensile Strength of Nextel 610 and 720 Fibres, *J. Mater. Sci.,* **32,** 2535-2542 (1997)

14. 3M Nextel Ceramic Fiber Technical Notebook, obtained from 3M Corporation website, Jun 2000

15. C.G. Levi, et. al., Processing and Performance of an All-Oxide Ceramic Composite, *J. Am. Ceram. Soc.*, **81** [8], 2077-86 (1998)

16. G.V. Franks, B. V. Velamakanni, and F. F. Lange, "VibraForming and In-situ Flocculation of Consolidate, Coagulated Alumina Slurries," *J. Am. Ceram. Soc.*, **78** [5] 1324-28 (1995).

17. W. C. Tu and F. F. Lange, "Liquid Precursor Infiltration and Pyrolysis of Powder Compacts, I: Kinetic Studies and Microstructure Development," *J. Am. Ceram. Soc.*, **78** [12] 3277-82 (1995)

18. W. C. Tu and F. F. Lange, "Liquid Precursor Infiltration and Pyrolysis of Powder Compacts, II, Fracture Toughness and Strength," *J. Am. Ceram. Soc.*, **78** [12] 3283-9 (1995)

19. E.P. Popov, "Mechanics of Materials, 2nd Edition," Prentice-Hall, 1976

20. J.A. Blind, J.P. Solti and M.W. Yocum, "Introduction to Mechanics: An Integration of Materials and Statics, 4th Edition," Forbes Custom Publishing, 1999

21. A.S. Saada, "Elasticity: Theory and Applications," Pergamon Press, 1974

22. S.P. Timoshenko and J.N. Goodier, "Theory of Elasticity, 3rd Edition," McGraw-Hill, 1970

23. S. Timoshenko and S. Woinowsky-Krieger, "Theory of Plates and Shells, 2nd Edition," McGraw-Hill, 1959

24. M. Goland and E. Reissner, "The Stresses in Cemented Joints," *ASME Journal of Applied Mechanics*, **11**, A17-A27 (1944)

25. C. Yang and S-S Pang, "Stress-Strain Analysis of Single-Lap Composite Joints Under Tension," *Journal of Engineering Materials and Technology*, **118**, 247-255 (1996)

26. L.J. Hart-Smith, "Adhesive-bonded Single-lap Joints," Douglass Aircraft Co., NASA Langley Research Center Report CR-112235 (1973)

27. I. Sneddon, "The Distribution of Stress in Adhesive Joints," Chapter 9 of *Adhesion*, by D.D. Eley, ed., Oxford University Press, Cambridge, U.K.

28. M-Y Tsai and J. Morton, "A Note on Peel Stresses in Single-Lap Adhesive Joints," *ASME Journal of Applied Mechanics*, **61**, 712-715 (1994)

29. R.C. Givler and R.B. Pipes, "Analysis of the 'Joggle-Lap' Joint for Automotive Applications," Joining of Composite Materials, ASTM STP 749, K.T. Kedward, Ed., American Society for Testing and Materials, 61-74

30. D.L. Logan, "A First Course in the Finite Element Method Using ALGOR," PWS Publishing Company, 1997

31. MSC/Patran Version 8, The MacNeal-Schwendler Corporation, Jan 1998

32. MSC/Nastran Version 7.5, The MacNeal-Schwendler Corporation, Jan 1998

33. G. Li, P Lee-Sullivan and R.W. Thring, " Nonlinear Finite Element Analysis of Stress and Strain Distributions Across the Adhesive Thickness in Composite Single-lap Joints," *Composite Structures*, **46**, 395-403 (1999)

34. H.L. Groth and D. Jangblad, "Fracture Initiation at Interface Corners in Bonded Joints," Paper presented at Euromech Colloquium 227, *Mechanical behaviour of Adhesive Joints*, Saint-Etienne, France, Editions Pluralis, Paris, 257 - 270 (1987)

35. T. Radsick, B. Saruhan and H. Schneider, "Damage Tolerant Oxide/Oxide Fiber Laminate Composites," *J. Eur. Ceram. Soc*, **20**, 545-550 (2000)

36. J.A. Heathcote, X.Y. Gong, J.Y. Yang, U. Ramamurty, F.W. Zok, "In-plane mechanical properties of an all-oxide ceramic composite," *J. Am. Ceram. Soc.*, **82** (10) 2721-2730 (1999)

Table 1

Item	Symbol	Value
Adherend Layer Thickness	t	0.24 mm
Overlap Distance	2c	1 cm
Young's Modulus of Adherend	E	75 GPa
Young's Modulus of Adhesive	E_c	30 GPa
Adhesive Layer Thickness	η	0.06 mm
Applied Average Stress	P	24.5 MPa
Stress Relief Factor	f	0.20

Table 1: Dimensions and material properties used in Tsai-Morton model of peel stress in a single-lap adhesive joint. Note the inclusion of a stress relief factor to improve the fit to the double-layer "Lap-Type" joint used later.

Table 2

Item	Value
Young's Modulus of CMC Layer	75 GPa
Young's Modulus of Matrix Layer	30 GPa
CMC Layer Thickness	0.18mm
Matrix Layer Thickness	0.03mm
Overlap Distance	1 cm
Applied Average Stress	24.5 MPa
Total Length	3 cm

Table 2: Dimensions and material properties used in finite element models of both the "lap-type" and the "joggle-type" joints.

Figure 1
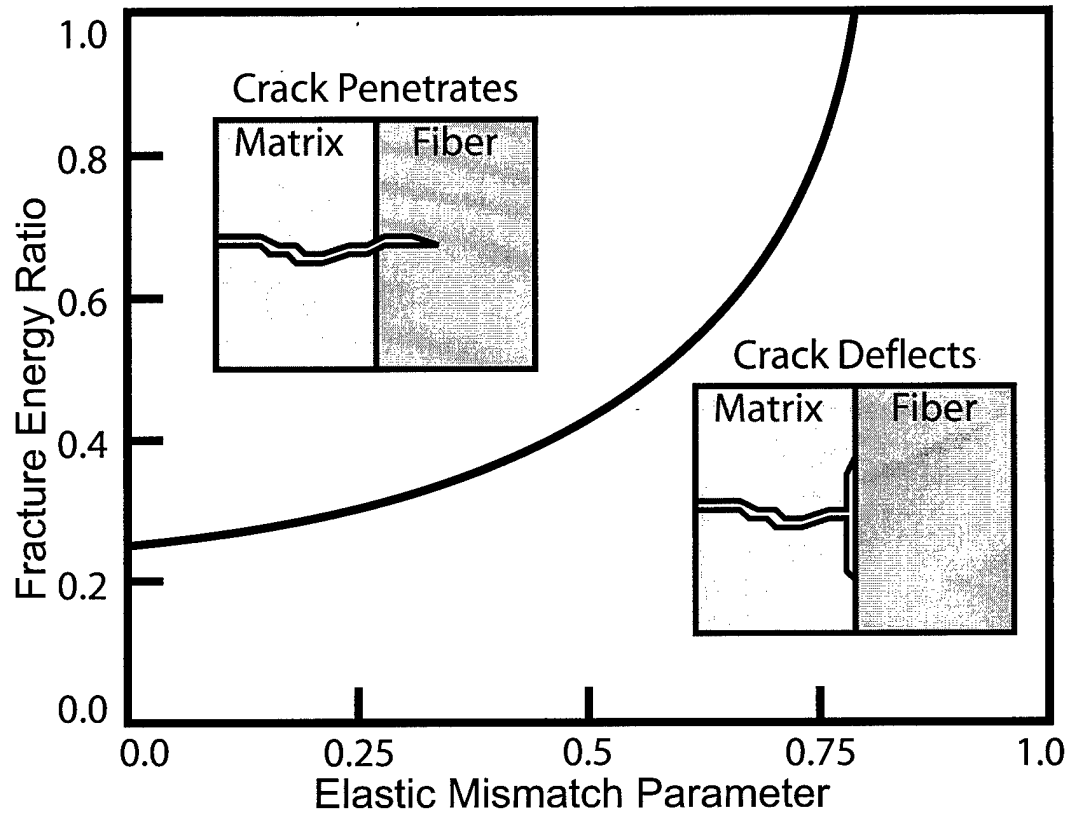
Figure 1: Plot of fracture energy ratio versus elastic mismatch parameter for an interface between two different materials (He and Hutchinson, 1989).

Figure 2
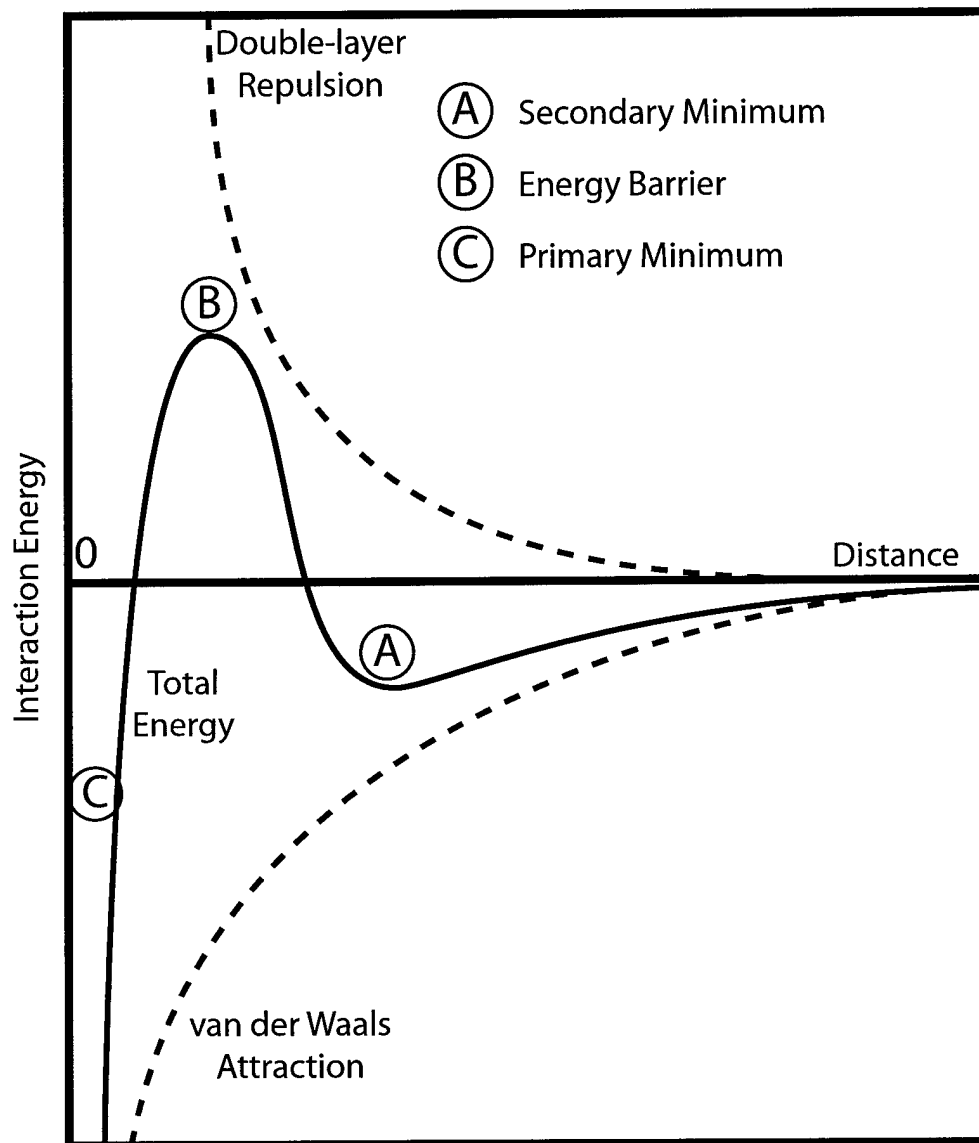
Figure 2: Interaction energy between two particles as a function of separation distance for DLVO Interaction at the critical coagulation concentration (Israelachvili, 1992).

Figure 3
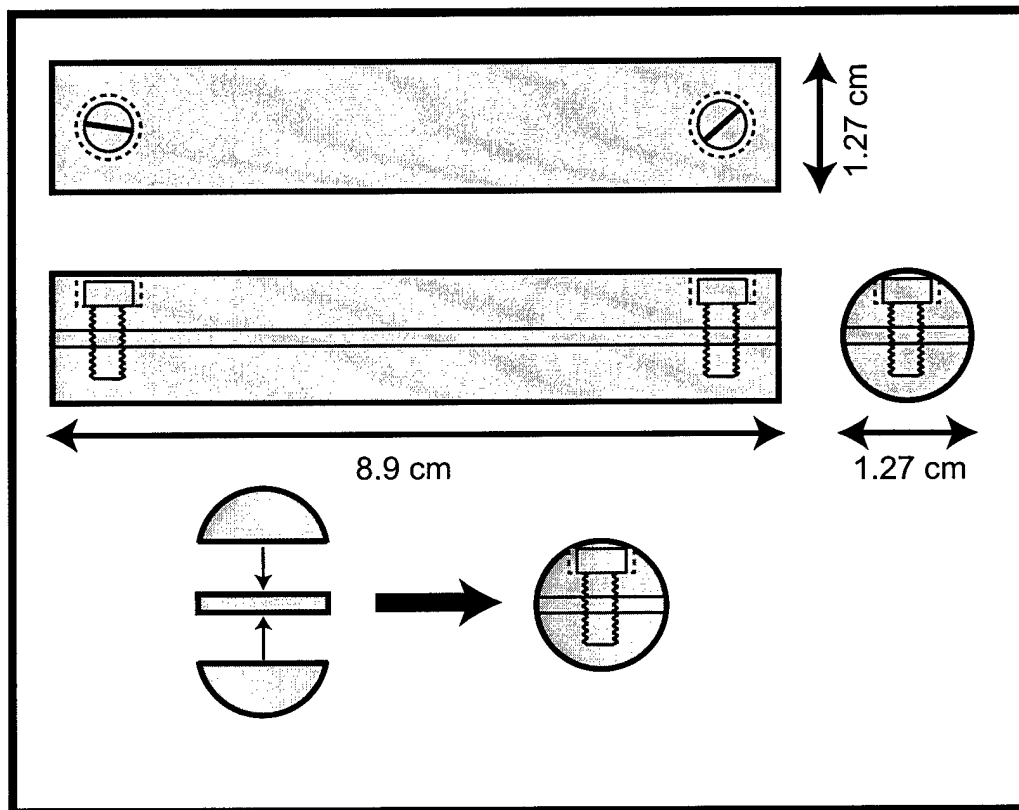
Figure 3: Orthographic schematic of the stainless steel mandrel used to fabricate the composite tubes in this study.

Figure 4
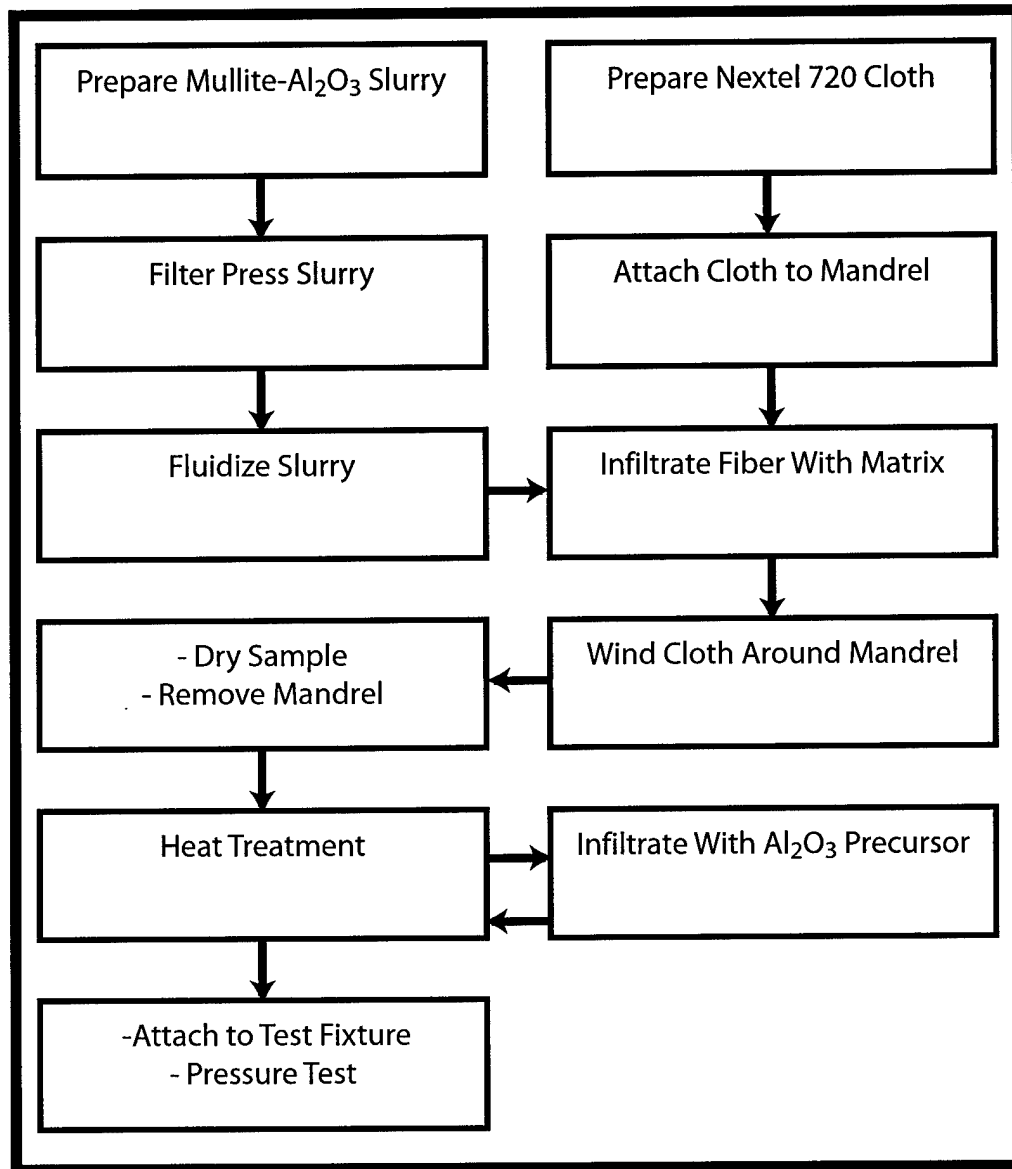
Figure 4: Flowchart of processing steps used to fabricate the composite tubes in this study.

Figure 5
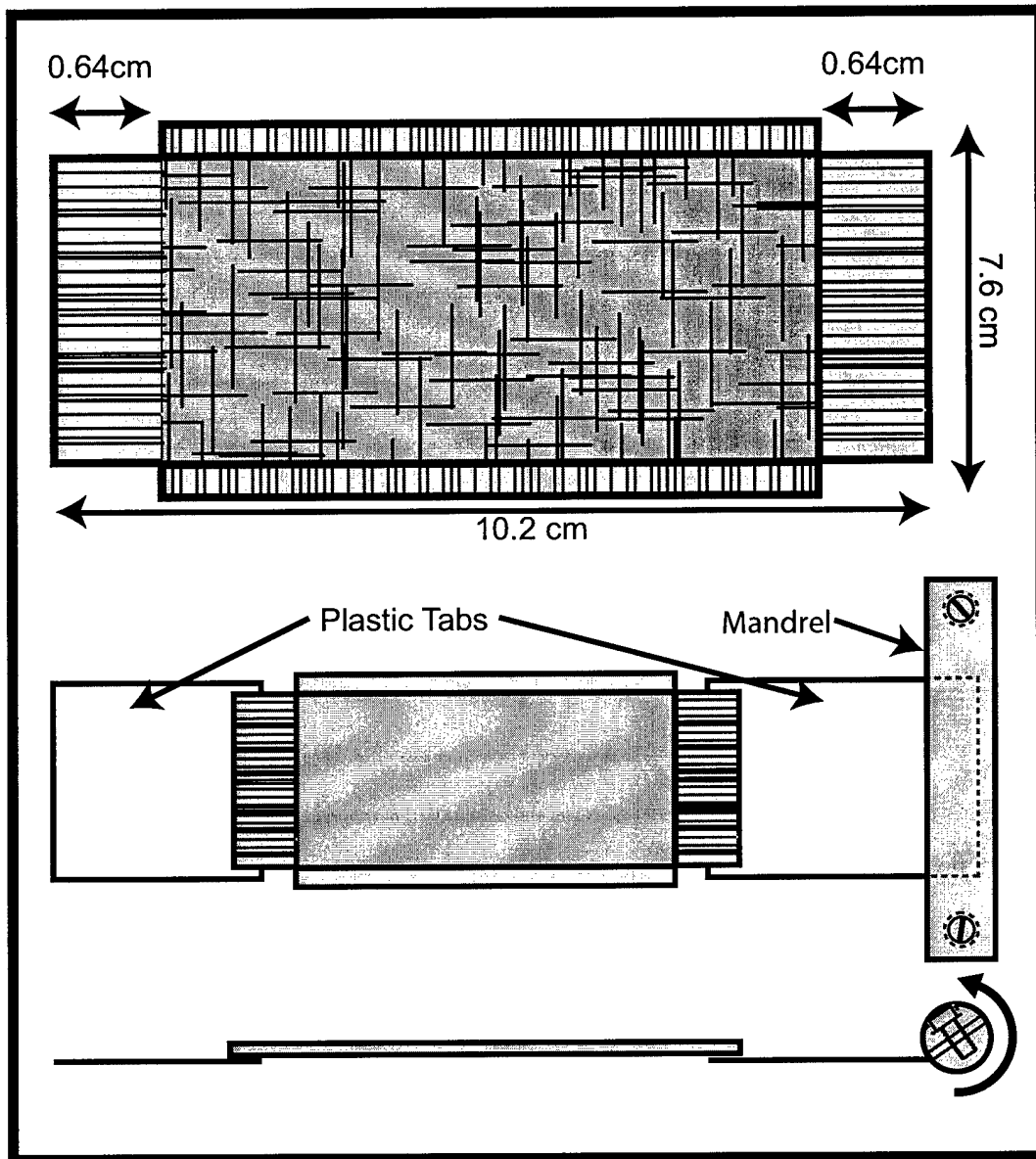
Figure 5: Diagram showing cloth dimensions and process used to fabricate tubes in this study. Plastic tabs were attached to the uninfiltrated fiber cloth using cyanoacrylate glue.

Figure 6
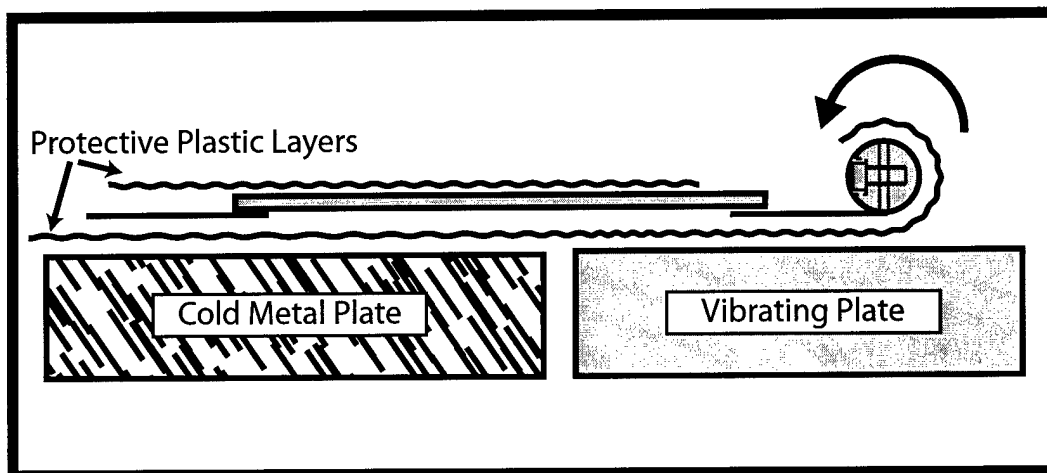
Figure 6: Equipment set-up for VibroIntrusion and rolling process. Infiltrated cloth layer was maintained in a frozen state on the cold plate, slid onto the vibrating plate to thaw out and become fluidized, and then rolled onto a mandrel.

Figure 7
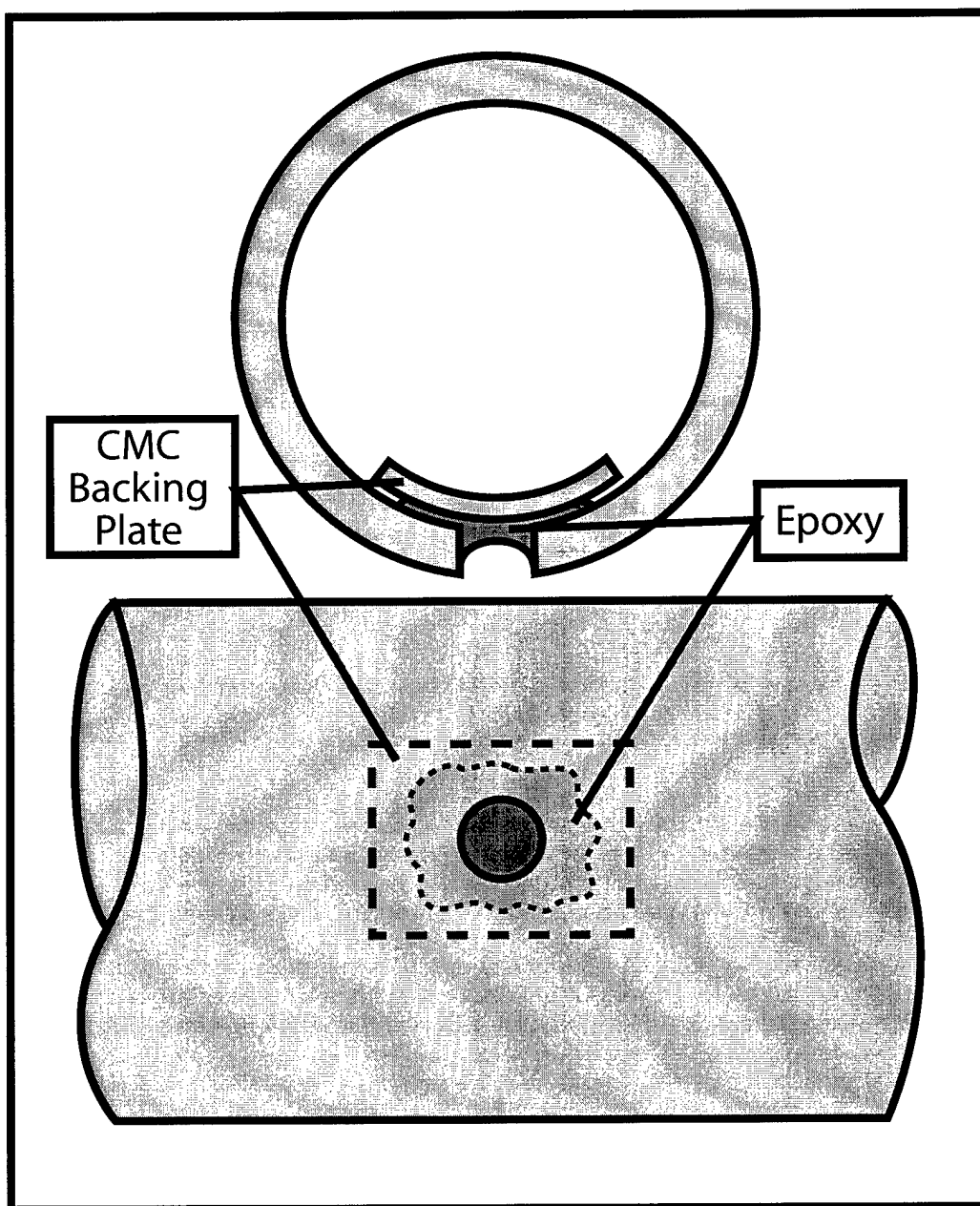
Figure 7: End view and side view of cored composite tube. Note the fillet of epoxy that extends into the cored hole.

Figure 8
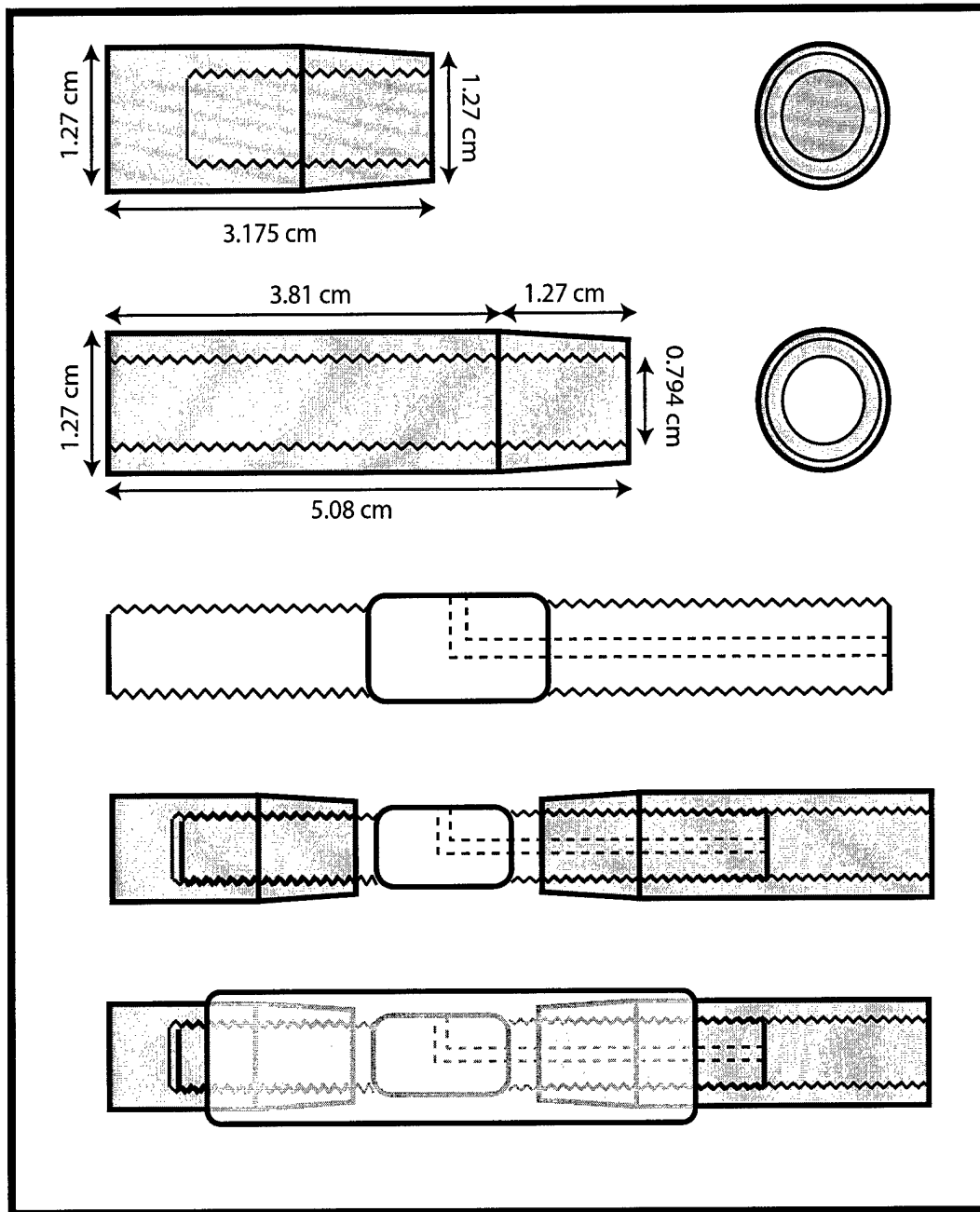
Figure 8: Orthographic schematic of the three-piece brass mandrel used to test the CMC tubes in this study. The mandrel with an attached CMC tube is also shown.

Figure 9
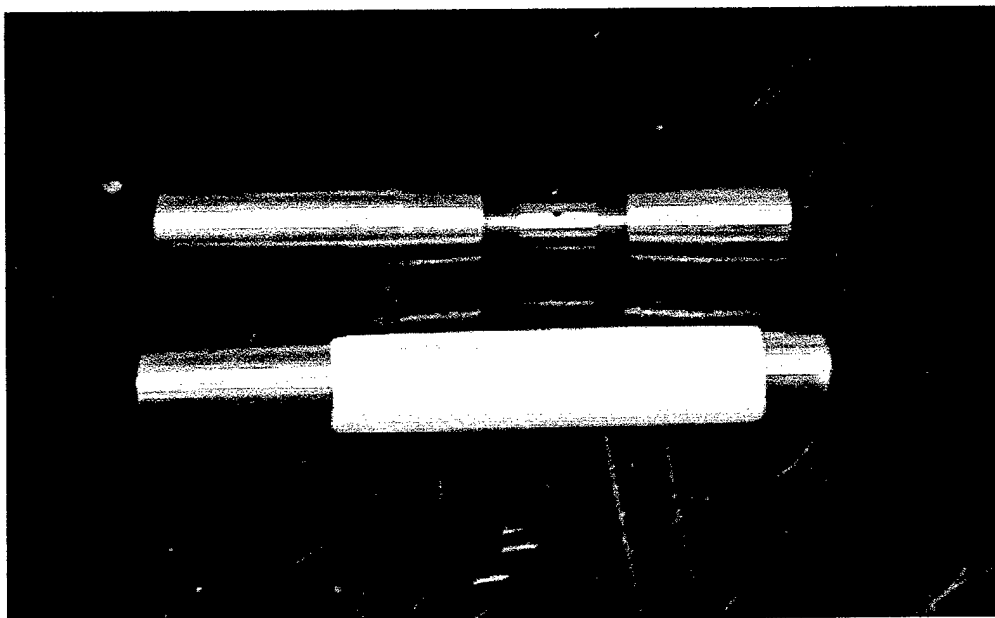
Figure 9: Photo of brass mandrel and mandrel with CMC tube attached.

Figure 10
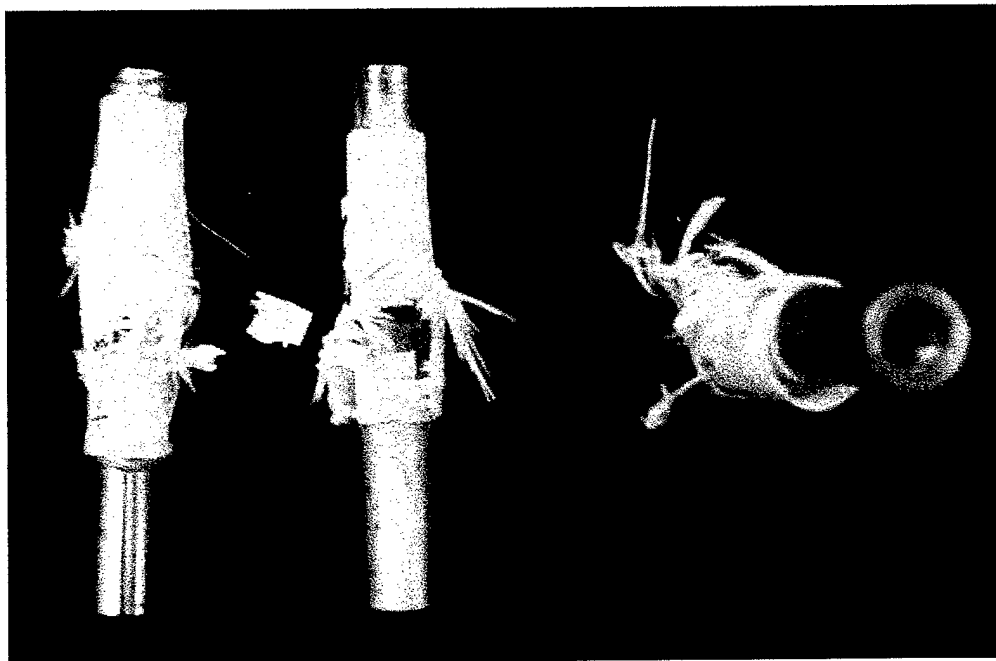
Figure 10: Photo of several CMC tubes after catastrophic burst testing.

Figure 11a
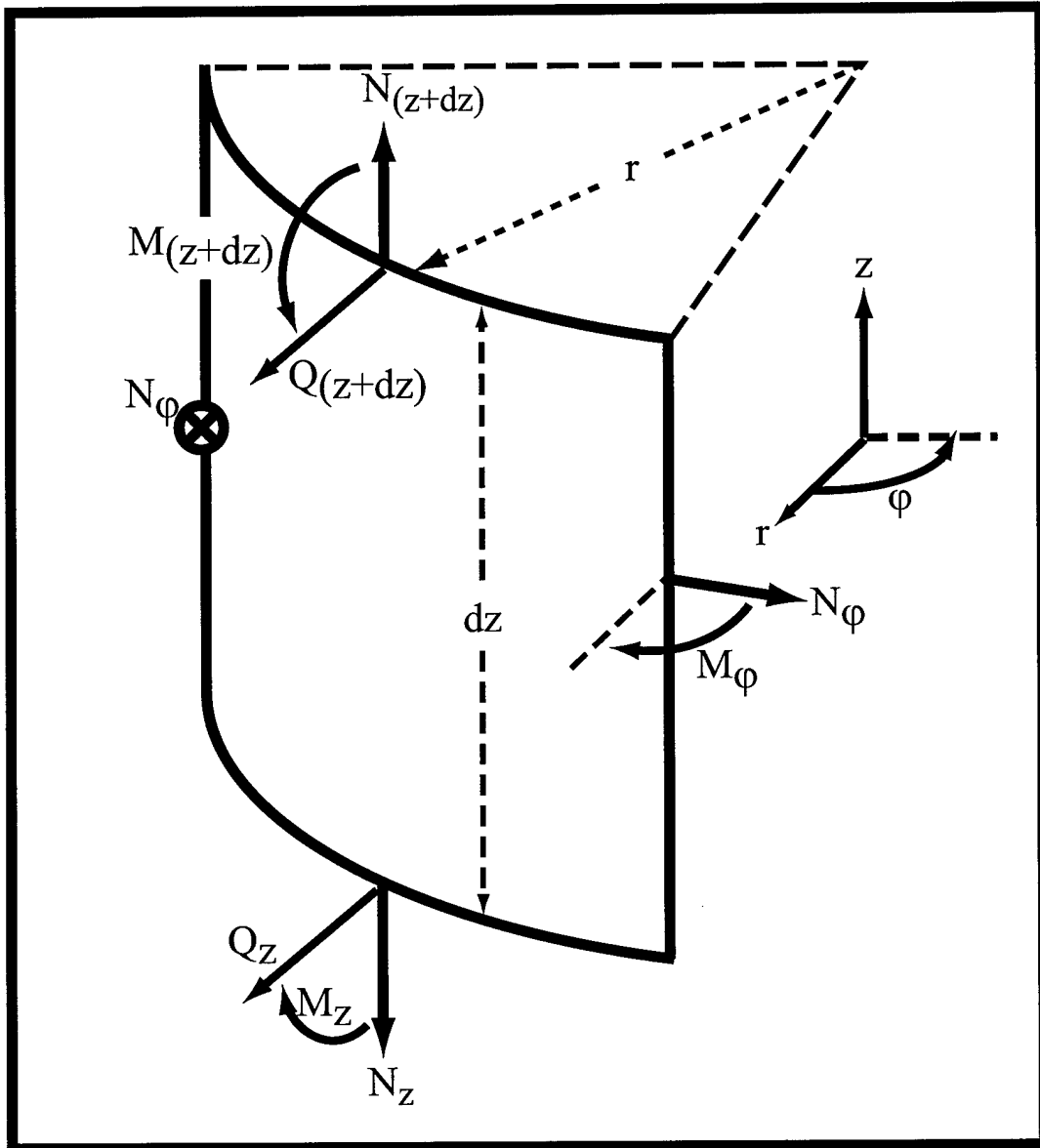
Figure 11a: Axis system and orientation of stresses and moments for an element of a CMC tube.

Figure 11b
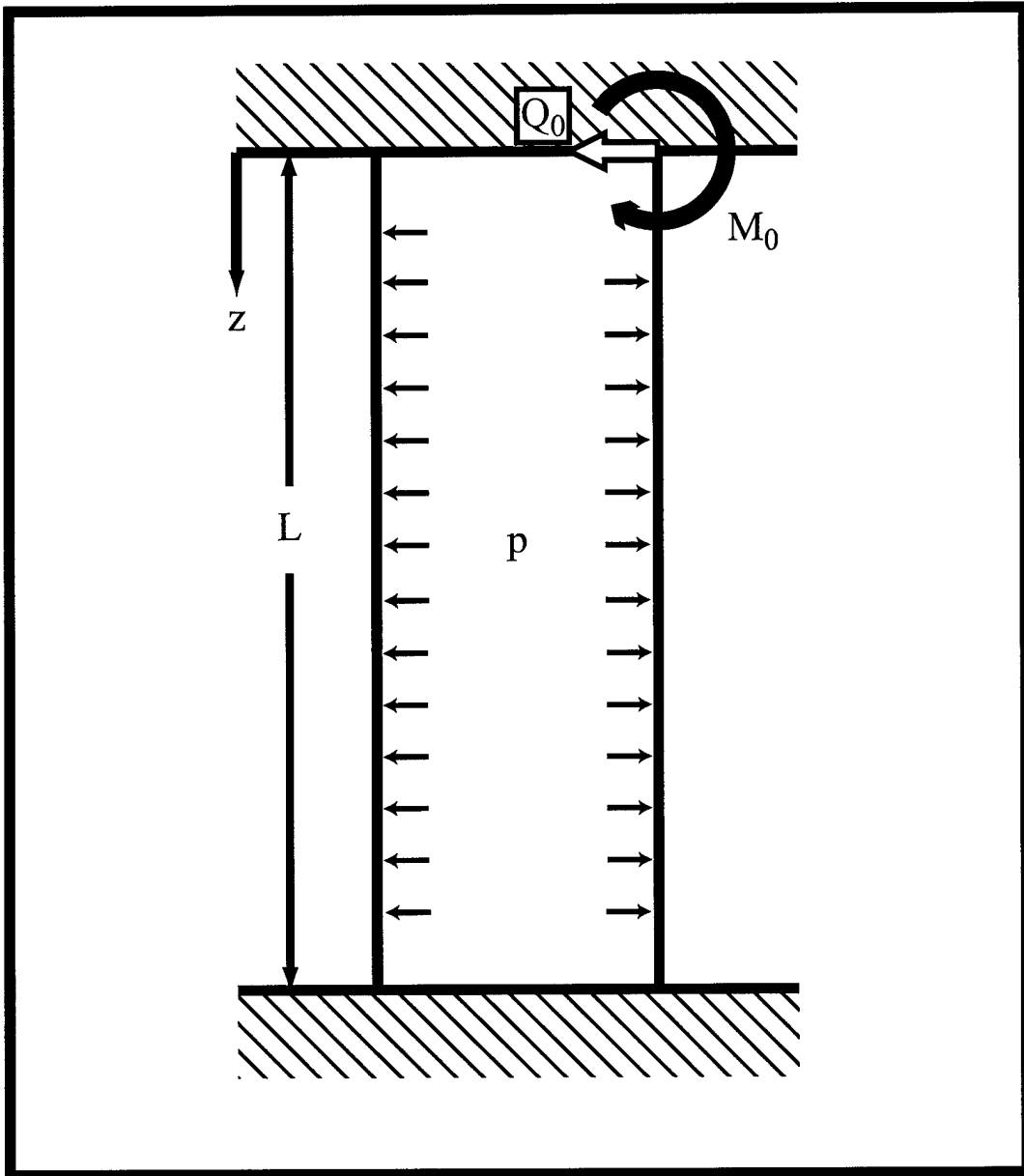
Figure 11b: Illustration of the built-in condition for a CMC tube.

Figure 12

Normal Stress for a "Built-In" CMC Tube
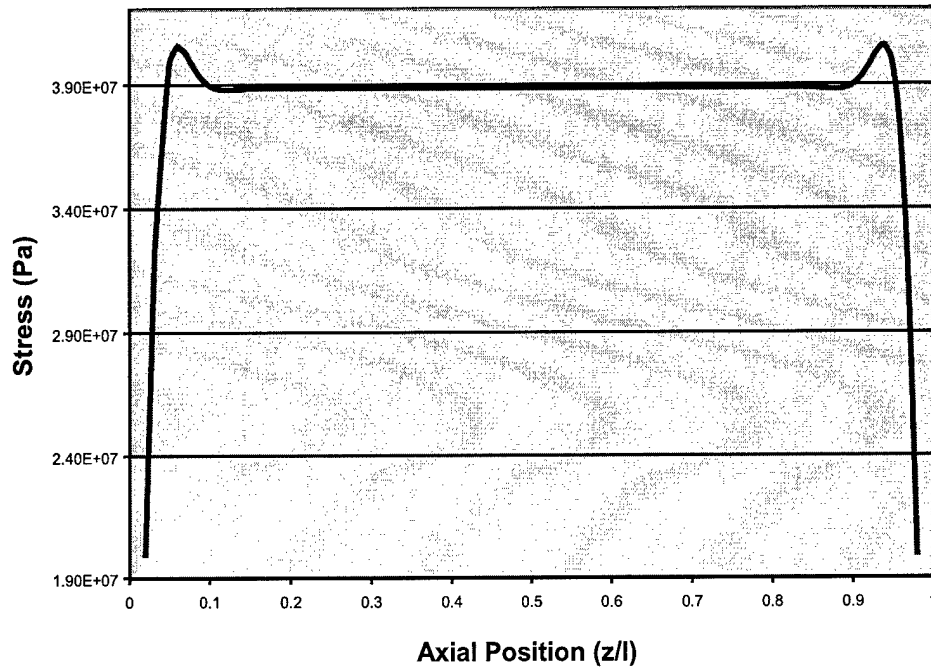
Figure 12: Normal stress versus axial position for the CMC tubes tested in this study. Stress shown is a result of the pressure applied at Failure Event 2. The effect of the built-in ends manifests as a 4% increase in the stress near each end.

Figure 13
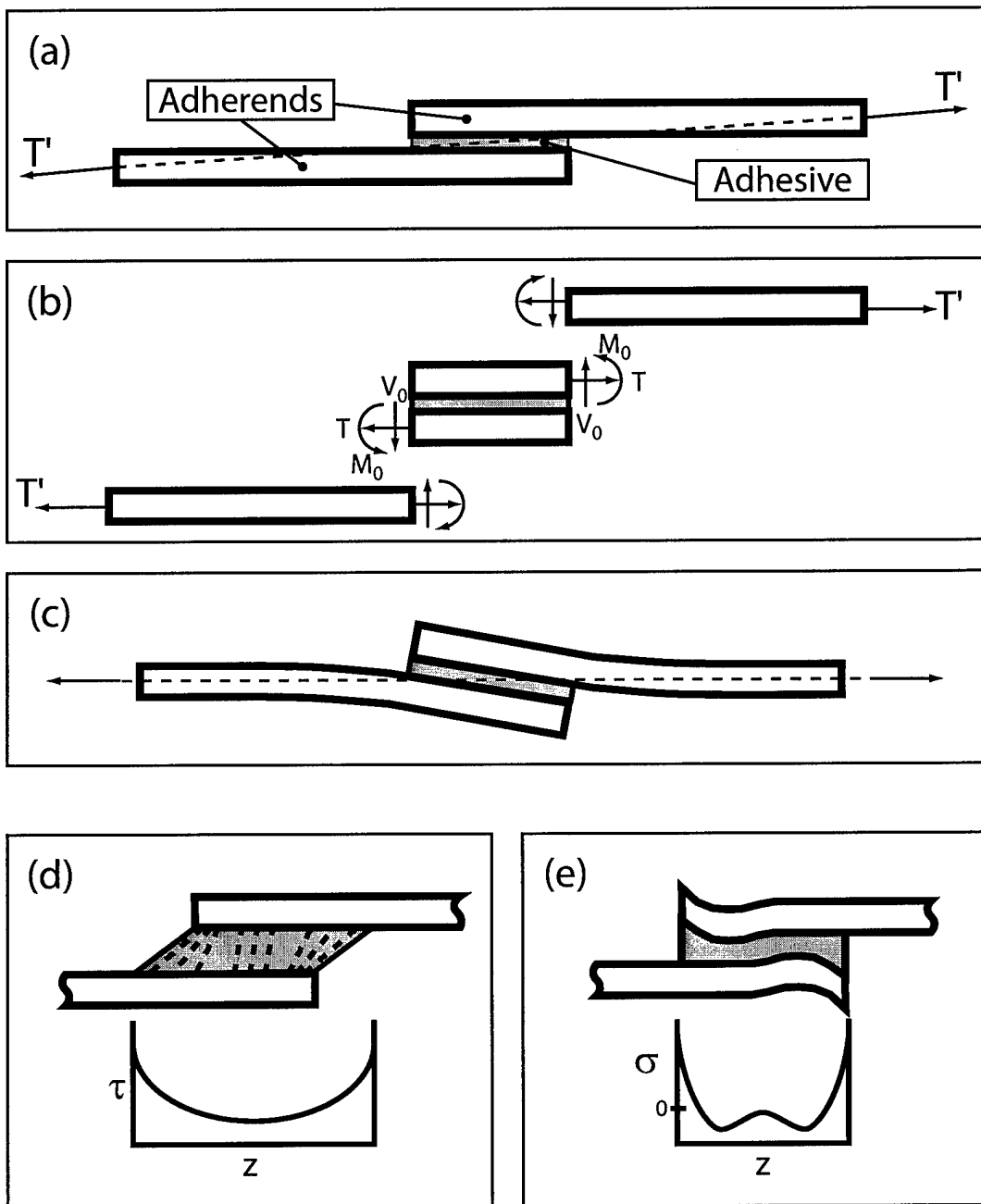
Figure 13: Single-lap joint configuration. (a) the general configuration of the single-lap joint and the skewed loading axis. (b) moments and forces expected in the joint overlap region. (c) deformation of the joint due to an applied load. (d) graphical illustration of the distribution of shear stress in the overlap region. (e) graphical illustration of the normal (peel) stress in the overlap region.
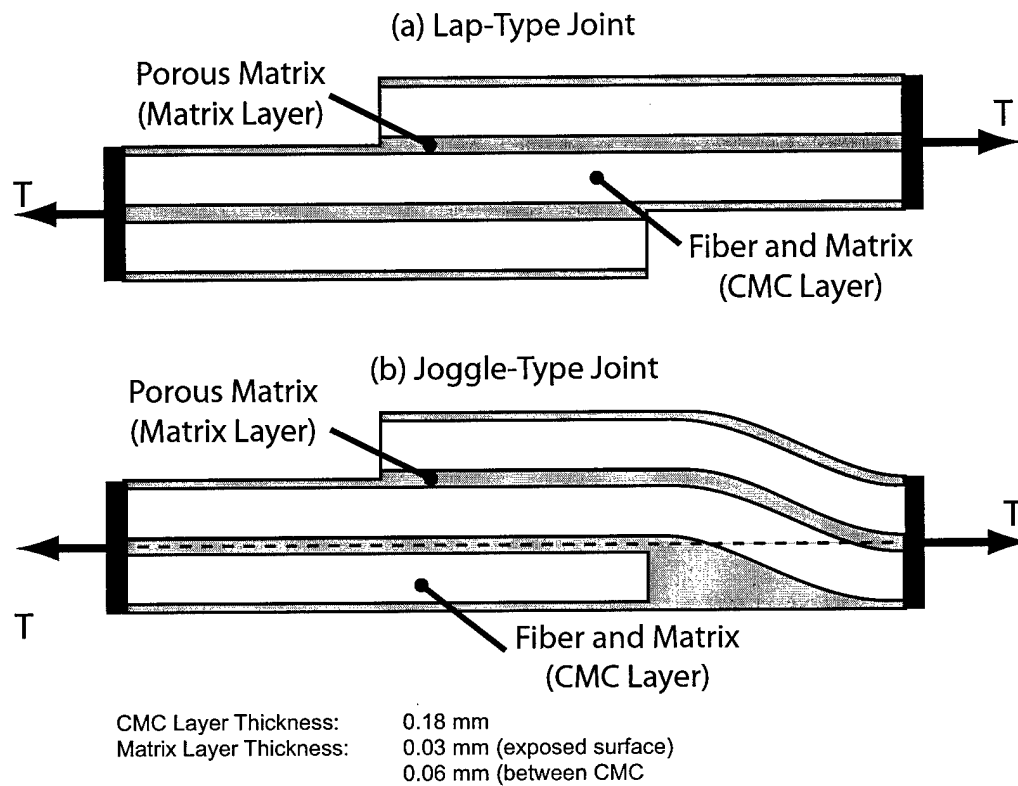
61

Figure 14

(a)

Adherends   Adhesive

T T

(b)

M_0 T

V_0

T V_0

T M_0 T

(c)

(d)

τ

z

(e)

σ

0

z

Figure 14: Joggle joint configuration. (a) the general configuration of the joggle joint and the skewed loading axis. (b) moments and forces expected in the joint overlap region. (c) deformation of the joint due to an applied load. (d) graphical illustration of the distribution of shear stress in the overlap region. (e) graphical illustration of the normal (peel) stress in the overlap region.

Figure 15

(a) Lap-Type Joint

Porous Matrix
(Matrix Layer)

Fiber and Matrix
(CMC Layer)

T

T

(b) Joggle-Type Joint

Porous Matrix
(Matrix Layer)

Fiber and Matrix
(CMC Layer)

T

T

CMC Layer Thickness:	0.18 mm
Matrix Layer Thickness:	0.03 mm (exposed surface)
	0.06 mm (between CMC

Figure 15: Lap-Type and Joggle-Type joints used in FEA models. Note that the thickness of the matrix layer in between two CMC layers is modeled as being twice the thickness of the matrix on the exposed surfaces.

Figure 16
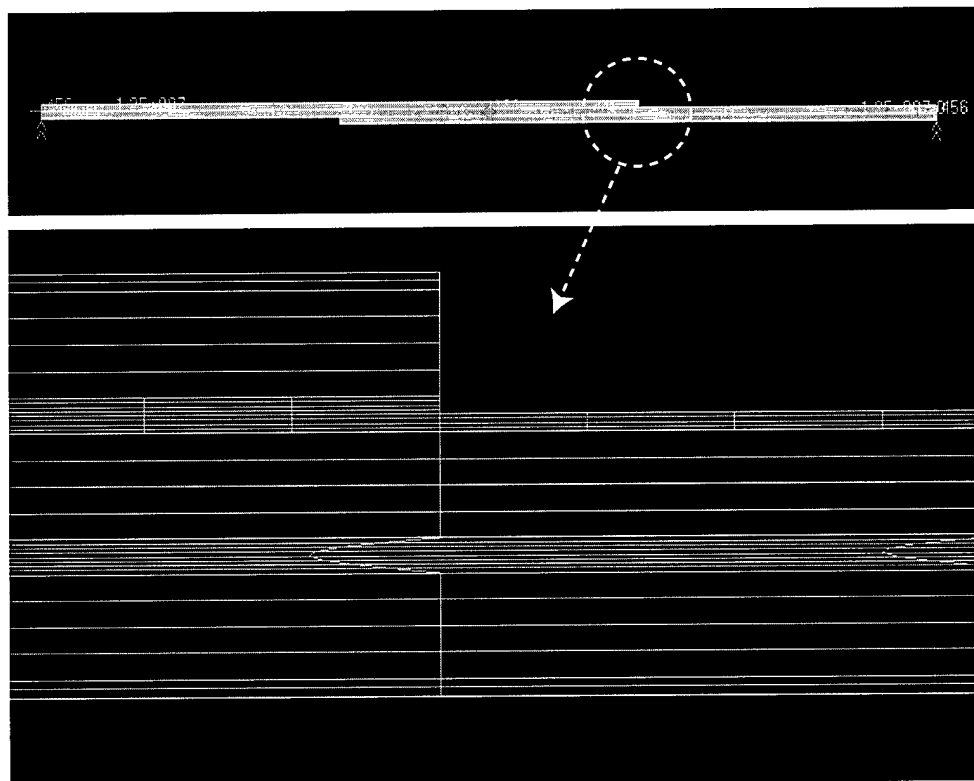
Figure 16: FEM mesh of portion of lap-type joint showing the mesh for a re-entrant corner.

Figure 17
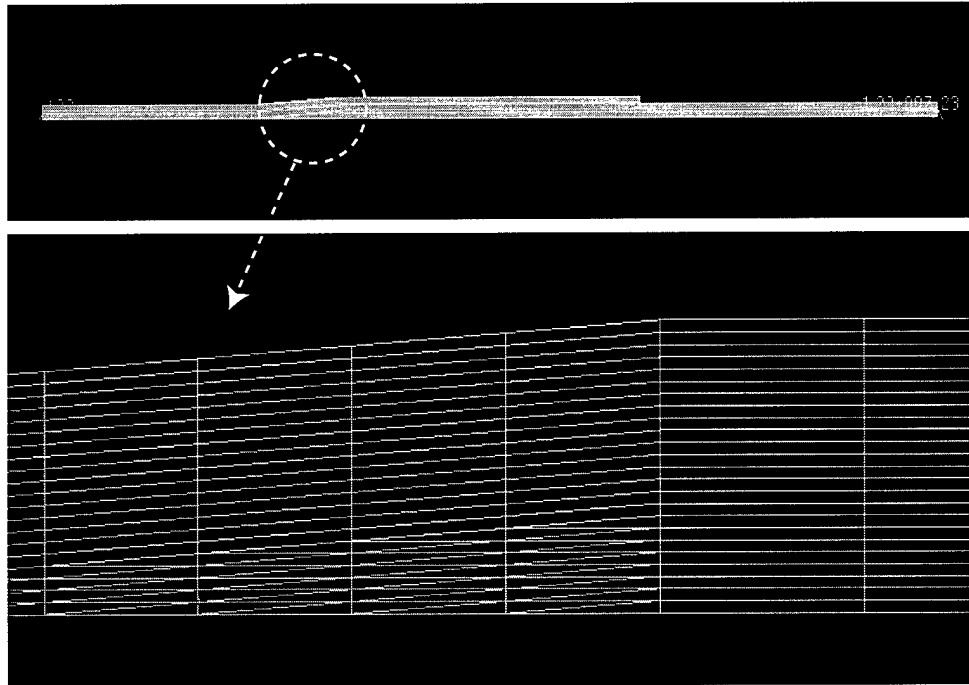
Figure 17: FEM mesh for joggle-type joint showing increased mesh density in the joggle region.
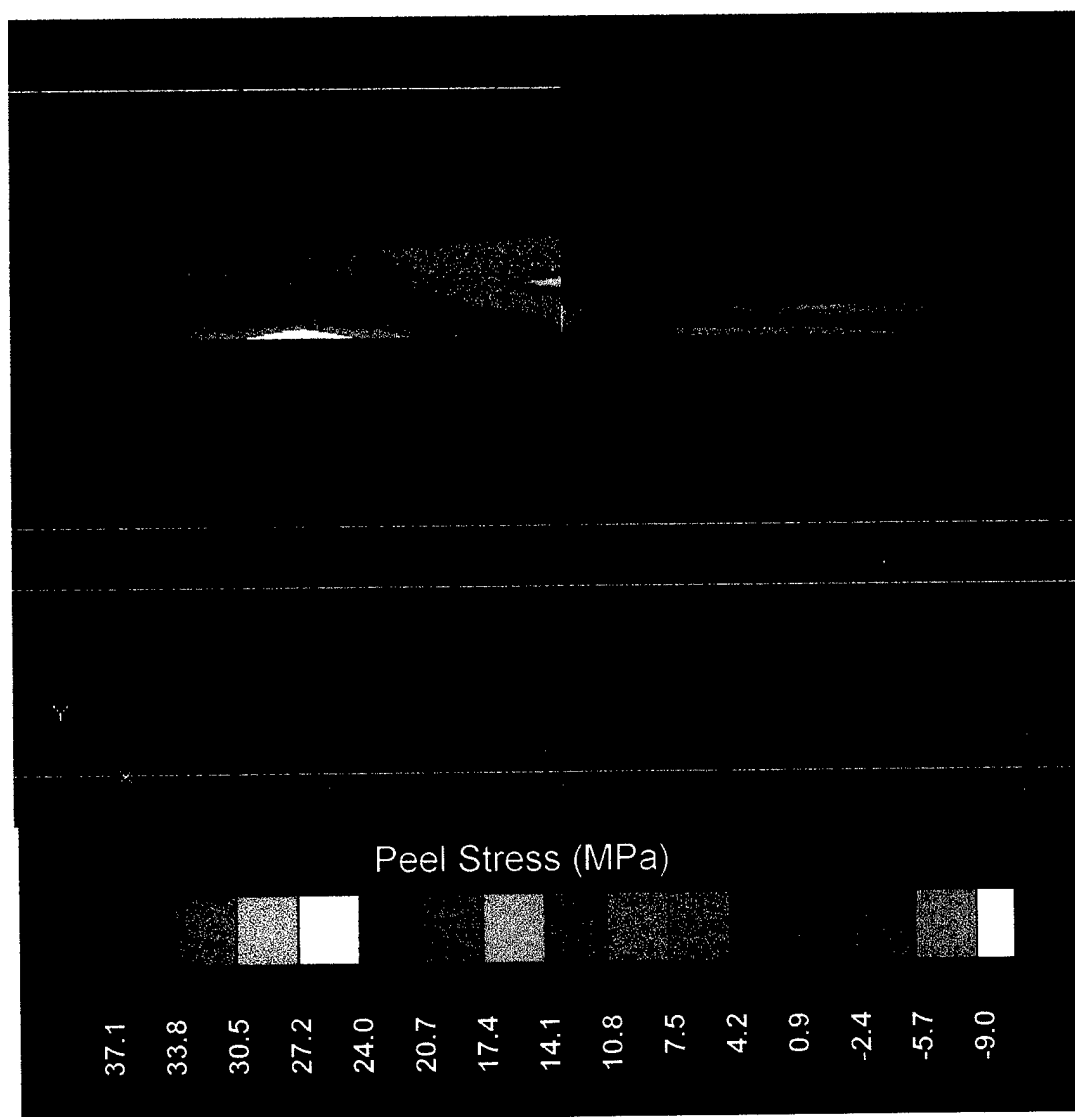
Figure 18a

Peel Stress (MPa)

37.1 33.8 30.5 27.2 24.0 20.7 17.4 14.1 10.8 7.5 4.2 0.9 -2.4 -5.7 -9.0

Figure 18a: FEA results for peel stresses in the re-entrant corner region of the lap-type joint. Maximum value of peel stress is approximately 16 MPa.
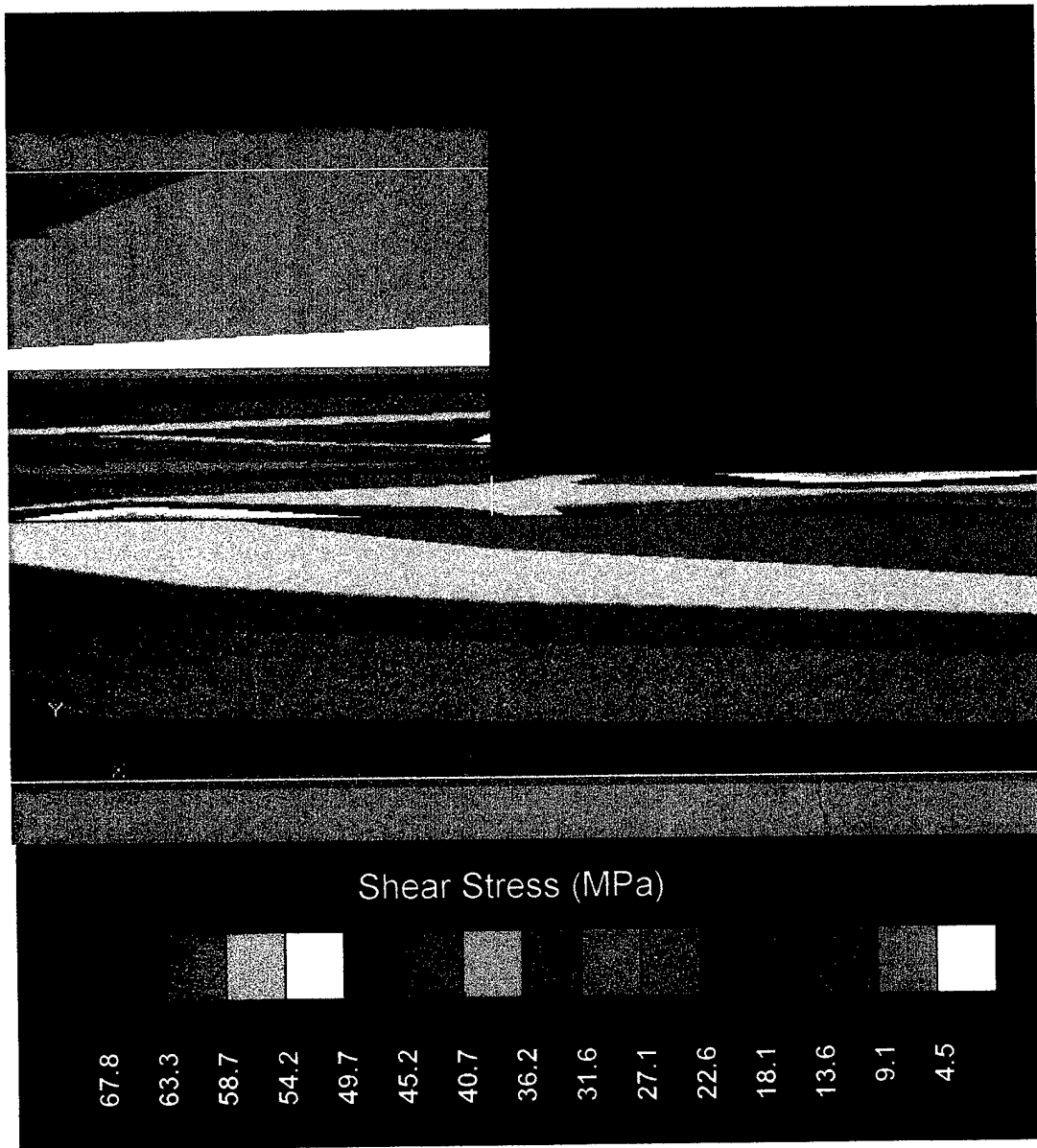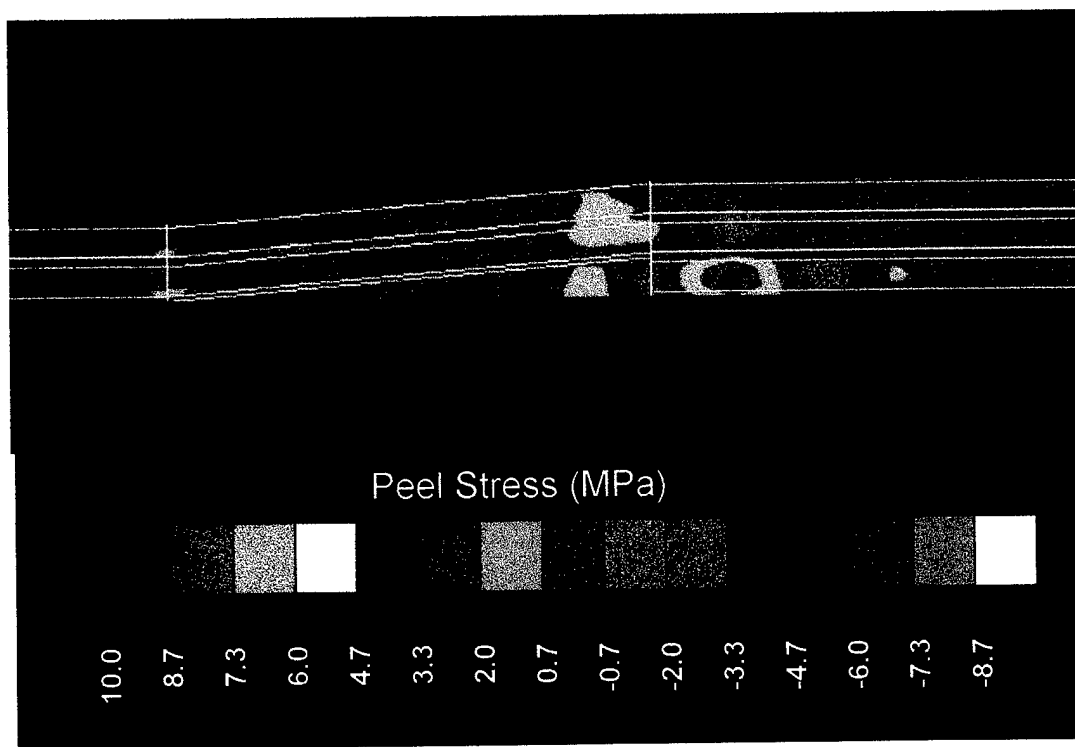
Figure 18b

Figure 18b: FEA results for shear stresses in the re-entrant corner region of the lap-type joint. Maximum value of shear stress is approximately 68 MPa.

Figure 19a

Figure 19a: FEA results for peel stresses in the joggle region of the joggle-type joint. Maximum value of peel stress is approximately 4 MPa.
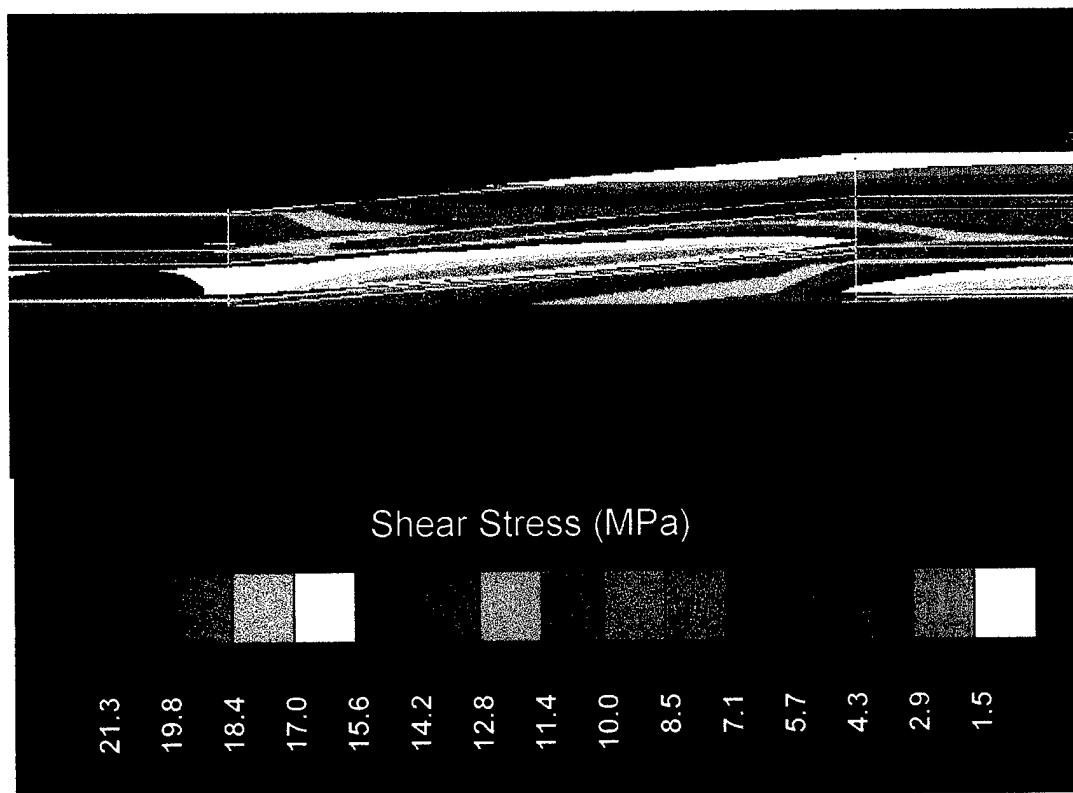
Figure 19b

Figure 19b: FEA results for shear stresses in the joggle region of the joggle-type joint. Maximum value of shear stress is approximately 20 MPa.

Figure 20

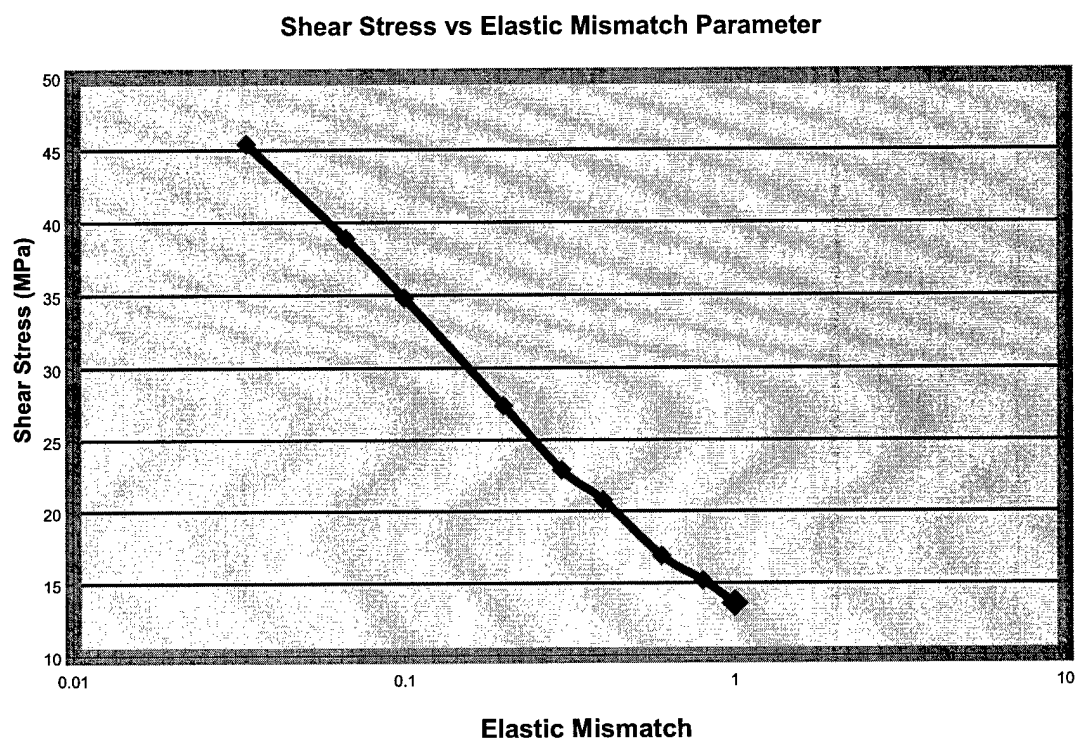**Shear Stress vs Elastic Mismatch Parameter**

Figure 20: Dependence of shear stress on ration between the Young's modulus of the CMC and matrix layers. In this plot, the modulus of the CMC layer was held constant at 75 GPa and the modulus of the matrix layer was varied. Note logarithmic scale on the abscissa.
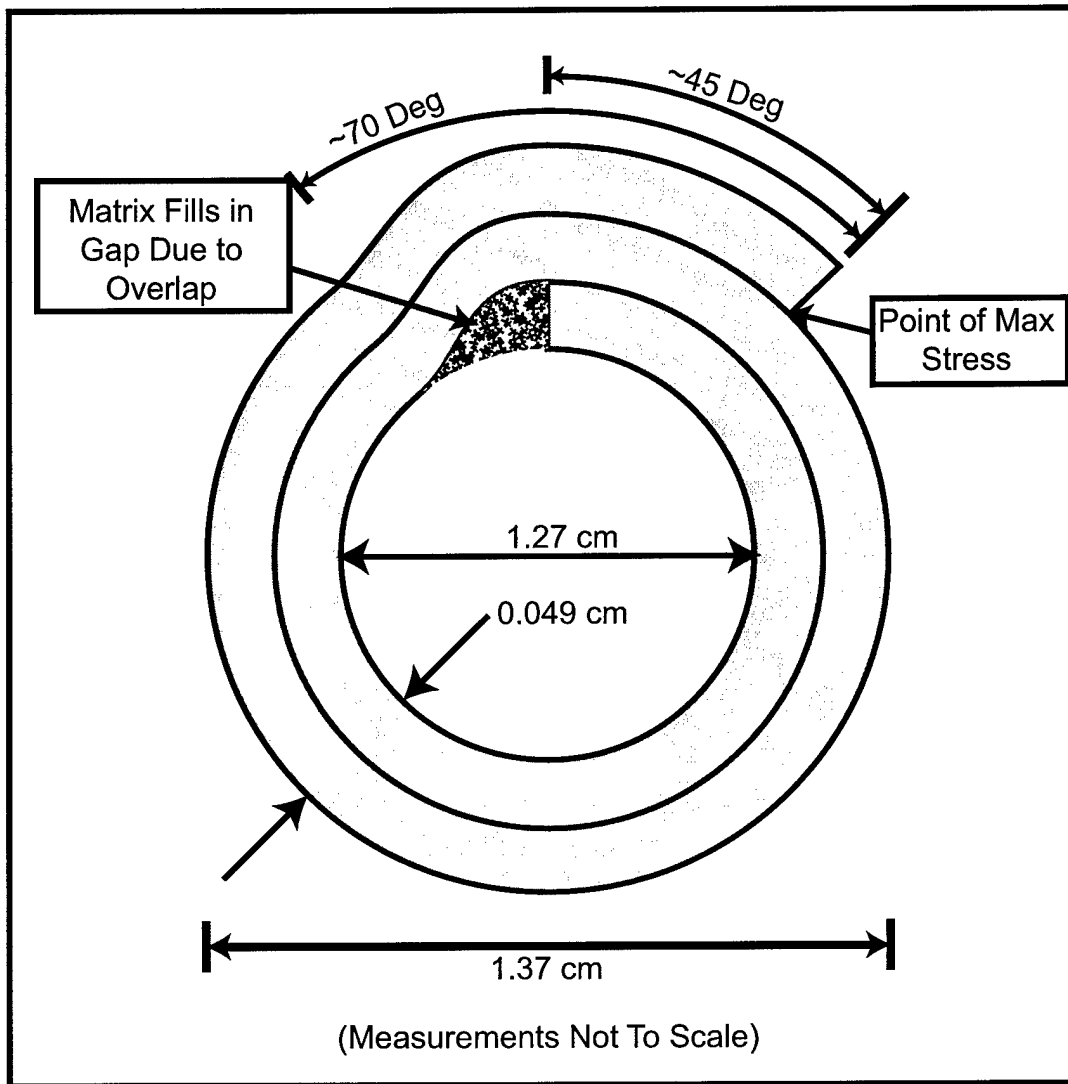
Figure 21

Figure 21: Cross-sectional view of CMC tube showing "jelly roll" configuration and filled-in joggle region.